minerals

MDPI

Article

Continental Arc Plutonism in a Juvenile Crust: The Neoproterozoic Metagabbro-Diorite Complexes of Sinai, Northern Arabian-Nubian Shield

Mohammed Z. El-Bialy [1], Mohamed Z. Khedr [2,*], Bassil M. El-Bialy [1] and Hatem F. Hassan [1]

[1] Geology Department, Faculty of Science, Port Said University, Port Said 42522, Egypt; mzbialy@sci.psu.edu.eg (M.Z.E.-B.); basel.elbially@sci.psu.edu.eg (B.M.E.-B.); hathassan@sci.psu.edu.eg (H.F.H.)
[2] Geology Department, Faculty of Science, Kafrelsheikh University, El-Geish Street, Kafrelsheikh 33516, Egypt
* Correspondence: mohamed.khader1@sci.kfs.edu.eg

Abstract: Based on new field, petrographic, and whole-rock geochemistry data, we investigated three discrete metagabbro-diorite complexes (MGDC) across the E-W Sinai to contribute to increasing knowledge of the evolution of the juvenile continental crust of the Neoproterozoic Arabian–Nubian Shield. The three MGDCs vary in the dominance of the gabbroic versus dioritic rock types among each of them. Gabbroids are distinguished into pyroxene-hornblende gabbros and hornblende gabbros, whereas dioritic rocks have been subdivided into diorites and quartz diorites. The studied MGDC rocks are almost metaluminous and possess prevalent calc-alkaline characteristics over subsidiary tholeiitic and alkaline affinities. The most distinctive feature in the profiles of the investigated MGDCs on the N-MORB-normalized spider diagrams is the coincidence of stout negative Nb anomalies and projecting positive Pb spikes, which is typical of igneous rocks evolved in subduction zones. The three MGDC samples exhibit variably LREE-enriched patterns [$(La/Yb)_N$ = 4.92–18.55; av. = 9.04], either lacking or possessing weak to negligible positive and negative Eu anomalies. The calculated apatite and zircon crystallization temperatures reveal the earlier separation of apatite at higher temperatures, with the obvious possibility of two genetic types of apatite and zircon in the magma (cognate vs. xenocrystic) since both accessories have yielded very wide ranges of crystallization temperatures. The investigated MGDCs were formed in a continental arc setting, particularly a thick-crust arc (>39 km). The parent magmas comprised components derived from the melting of the mantle wedge, subducting oceanic lithosphere, and subducting overlying sediments. The mantle input was from a spinel–garnet transitional mantle source at a depth of ca. 75–90 km. The impact of slab-derived fluids was much greater than that of slab-derived melts, and so subduction-related fluids had a crucial effect on metasomatizing the partially melted mantle source. The parent mantle-derived magma has been subjected to substantial crustal contamination as a dominant mechanism of differentiation.

Keywords: metagabbro-diorite complex; arabian-nubian shield; geochemistry; continental arc; mantle wedge metasomatism; subduction component

check for updates

Citation: El-Bialy, M.Z.; Khedr, M.Z.; El-Bialy, B.M.; Hassan, H.F. Continental Arc Plutonism in a Juvenile Crust: The Neoproterozoic Metagabbro-Diorite Complexes of Sinai, Northern Arabian-Nubian Shield. *Minerals* **2024**, *14*, 145. https://doi.org/10.3390/min14020145

Academic Editor: Silvana Martin

Received: 27 November 2023
Revised: 24 January 2024
Accepted: 26 January 2024
Published: 29 January 2024

Copyright: © 2024 by the authors. Licensee MDPI, Basel, Switzerland. This article is an open access article distributed under the terms and conditions of the Creative Commons Attribution (CC BY) license (https://creativecommons.org/licenses/by/4.0/).

1. Introduction

The Neoproterozoic basement rocks of Sinai and the Egyptian Eastern Desert (ED) constitute the northwestern margin of the exposed juvenile Neoproterozoic (550–900 Ma) crust of the Arabian-Nubian Shield (ANS) [1,2]. The ANS is considered the best-exposed and largest Neoproterozoic juvenile continental crust on Earth [1–6]. The ANS represents a collage of accreted arc and back-arc terranes following the closure of the Mozambique Ocean and the collision between East- and West-Gondwana. Growth of the ANS juvenile crust occurred all over most of the Neoproterozoic Era (900–600 Ma; [1]) through three main stages, viz.: (1) accretion stage (870–670 Ma) comprising the formation and amalgamation of arc terrains onto East Gondwana continental block [1,2,6–8]; (2) collision (650–630 Ma)

between the accreted juvenile ANS crust with the ancient pre-Neoproterozoic Saharan Metacraton (i.e., the continental margin of West Gondwana) along arc–continental and arc-arc sutures [9,10], and (3) post-collisional stage (620–580 Ma), initiated after cessation of collision, and involved extensional collapse of the thickened lithosphere, inducing extension and thinning of the ANS crust [11–15].

The Gabbroic rocks of the Neoproterozoic ANS of Egypt evolved in disparate tectonic regimes, and each has its own distinct geochemistry and petrogenesis. They were formerly classified into two main groups: older metagabbros and younger fresh gabbros [16,17]. Younger gabbros are typically tholeiitic-calc-alkaline intrusive mafic rocks (e.g., olivine gabbro and related rocks) that evolved in a post-collisional setting [18–25]. Older metagabbros are either an essential part of the oceanic lithosphere (ophiolitic tholeiitic gabbros) or arc-type calc-alkaline metagabbro–diorite complexes [26,27]. Exclusive of whole-rock geochemistry, the differentiation between the ophiolitic metagabbros and those formed in volcanic arcs (metagabbros–diorite complex) is difficult since both are petrographically identical, deformed, and regionally metamorphosed up to greenschist/lower amphibolite facies [26,28].

Recent studies on the metagabbro-diorite complexes (MGDC) are limited both in the Eastern Desert (e.g., [29–35]) and Sinai (e.g., [19,36–38]). The metagabbro-diorite complex rocks are of widespread distribution in the Precambrian Egyptian basement relative to the post-collisional gabbros. They occur as rather large outcrops covering vast areas in the central and southern segments of the Eastern Desert; for instance, the mass outcropping west of Marsa Alam (≈1400 km^2 area) extends from Gabal Atud in the south to Wadi Mubarak in the north. The complexes are generally variable in composition, yet some are utterly gabbroidal (e.g., El-Aradiya; [39]). The gabbroic rocks comprise hornblende gabbro, pyroxene-hornblende gabbro, quartz-hornblende gabbro, and amphibolite. Along with diorites and quartz diorites as felsic members, scarce tonalities, granodiorites [34,40,41], and pyroxene diorites [32] are reported. In the Eastern Desert, MGDC rocks intrude the ophiolitic assemblages, arc-type metavolcanics, and metasediments, and on the contrary, they are intruded by the arc Older Granites, Younger Granitoids, and the post-collisional younger gabbros (e.g., [32,39,41,42]). In Sinai, they show the same chronological relations except for ophiolitic rocks and post-collisional gabbros due to the absence of the former in Sinai and spatial non-coexistence with the latter.

The initially reported absolute ages for the metagabbro-diorite complexes were K-Ar whole-rock and hornblende and biotite ages from the north Eastern Desert (NED) (881 ± 58 Ma; [40]) and Sinai (794 ± 30 Ma; [43]), respectively. Recent more precise U-Pb zircon dating for MGDC rocks revealed diverging ages spanning the Ediacaran (632 ± 4 Ma for Shahira gabbro-diorite intrusion, Sinai; [4]), Cryogenian (694.5 ± 2.1 Ma for two diorites and 695.3 ± 3.4 Ma for one gabbronorite from G. Atud, Eastern Desert; [33]), and Tonian (1017 ± 5 Ma for El-Fringa metagabbro, Sinai; [5]) and 728 ± 4 Ma for Um Balad gabbro-diorite complex NED, [35]).

The arc-type metagabbro-diorite rocks of the juvenile ANS crust are generally poorly studied, particularly those in Sinai. The present study deals with the rocks of three metagabbro-diorite complexes extending along the Sinai Precambrian massive, namely, Wadi Ba'aba'a, Wadi Harqus, and Gabal Shahira areas located in the western, central, and eastern Sinai, respectively (Figure 1). Except for Shahira MGDC (e.g., [36]), almost no geological information was presented on the other couple of metagabbro-diorite complexes. In this contribution, we present the results of new field, petrographic, and whole-rock major, trace, and rare earth element data on these three discrete metagabbro-diorite complexes in Sinai. These new data have been used to better understand the petrogenesis and tectonic evolution of the Neoproterozoic mafic plutonism in the northern segment of the Arabian-Nubian Shield and to constrain the nature of the magma source along with the various processes involved in its petrogenesis.

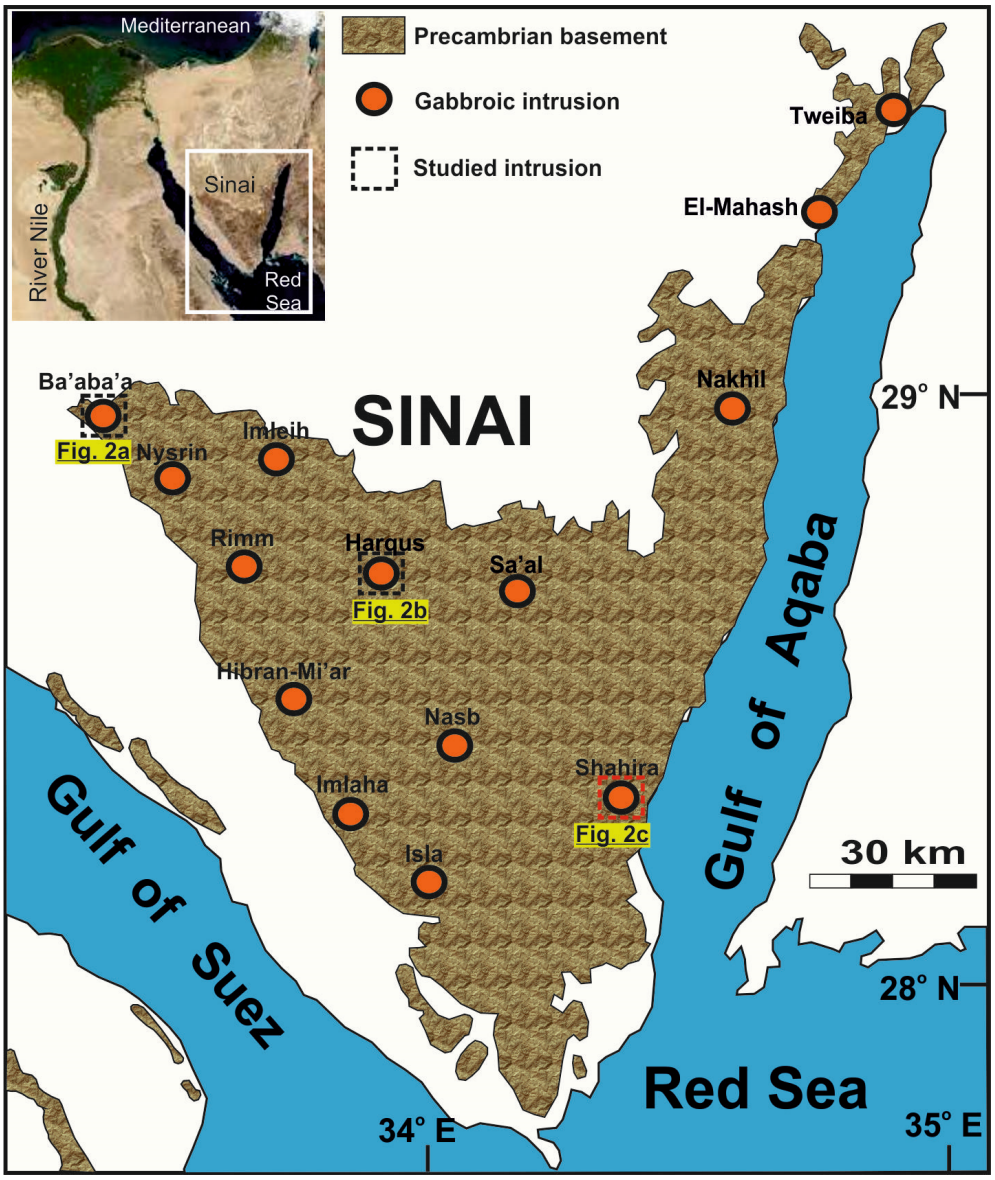


Figure 1. Location of the major late Neoproterozoic gabbroic intrusions within the Precambrian basement of Sinai. The three studied metagabbro-diorite complex intrusions (Figure 2) are bound by dashed squares. The inset map shows the location of the mapped area.

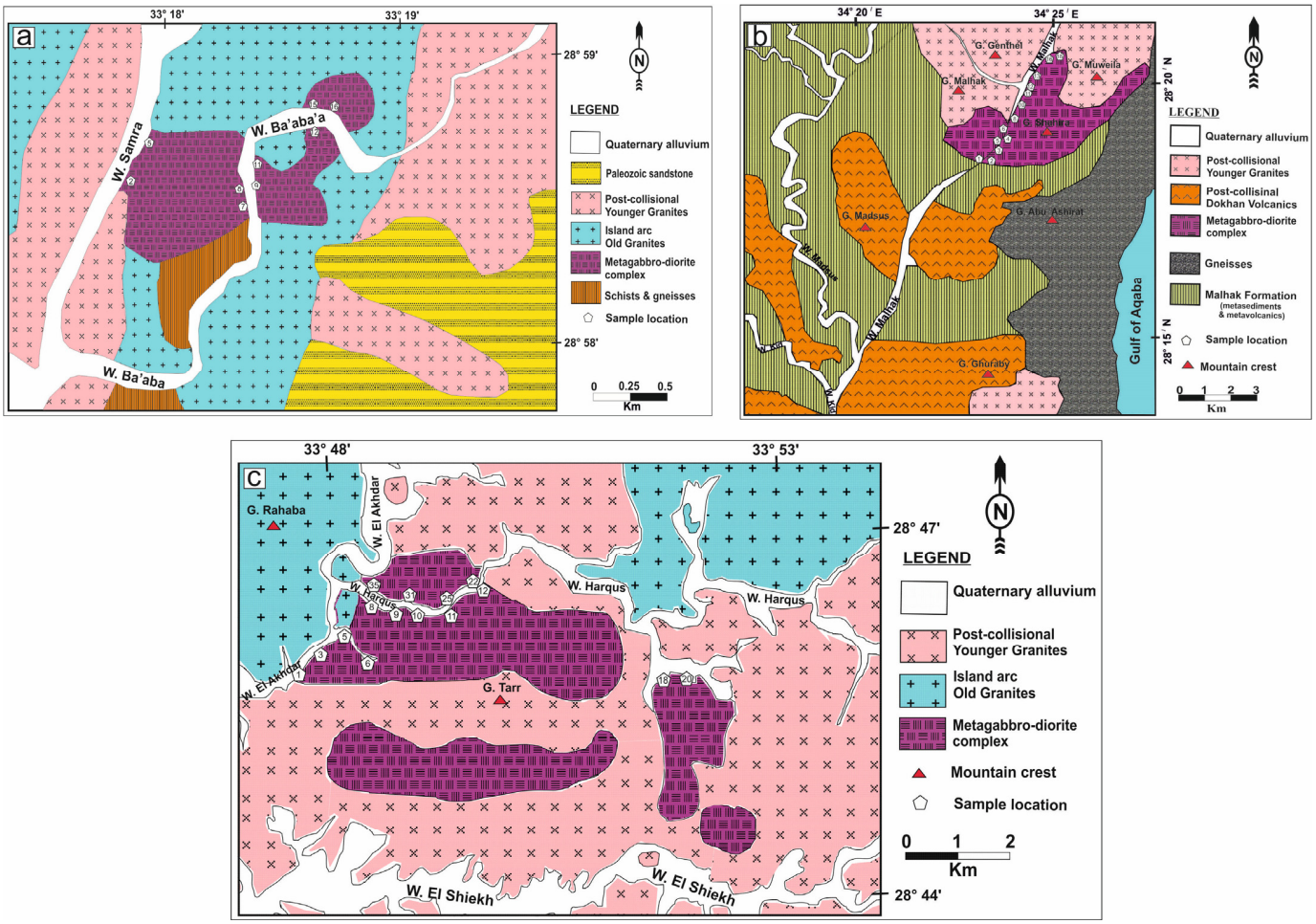


Figure 2. Simplified geological maps of the areas comprising the investigated metagabbro-diorite complexes: (**a**) W. Ba'aba'a, (**b**) G. Shahira, and (**c**) W. Harqus.

2. Geological Setting of the MGDC-Hosting Areas

A brief account of the geological setting of the three areas hosting the investigated metagabbro-diorite complexes is given in this section. This includes a description of the different rock units exposed in these areas with regard to the most diagnostic lithologic characteristics, contact relationships, and relative age relationships as revealed in the field. Modified geological maps were constructed for these areas based on former maps and careful checkups during the fieldwork.

2.1. Wadi Ba'aba'a Area

This area occupies the northwestern extremity of the exposed basement rocks of the southern Sinai, a few kilometers east of the Gulf of Suez coast. It is a mountainous terrain that is mainly covered by a Precambrian crystalline basement of metamorphic and igneous rocks and an overlaying clastic succession of Paleozoic sandstones (Figure 2a). The landscape is dominated by moderate relief, ranging between 100 m and 700 m above sea level, and the main streams dissecting the area are Wadi Ba'aba'a and Wadi Samra. Apart from several dykes of different ages and compositions cutting through, the Precambrian basement succession of this area is believed to be as follows from old to young [44]: Schists and gneisses; the Metagabbro-diorite complex (BMGDC); Island arc Old Granites; and Post-collisional Younger Granites.

Schists and gneisses occur as two mountainous masses extending along both banks of the Wadi Ba'aba'a lower course (Figure 2a). Schists, particularly mica schists, are dominant in this unit rather than the gneisses. Metamorphic structural elements such as foliation,

different types of lineation, and minor folds are quite common. These rocks are intruded by the Old and Younger granitoids as well as the metgabbro-diorite complex rocks.

The metagabbro-diorite complex is exposed as a belt extending from the eastern side of Wadi Samra and crossing both sides of Wadi Baba. It is mainly represented by melanocratic diorites that pass into more basic gabbro with gradational diffused contact. They are coarse- to medium-grained granular rocks. These rocks intrude the gneisses and schists, which in turn are intruded by the two granitoid suites with sharp contacts. Variably sized xenolithic masses and rafts of metagabbro-diorite complex rocks are usually observed within the marginal and contact zones of the Old Granites along Wadi Samra and Wadi Ba'aba'a (Figure 3a). Younger Granites also intrude the metagabbro-diorite complex rocks with sharp contact (Figure 3b), which is occasionally characterized by the presence of angular undigested xenoliths of the latter.

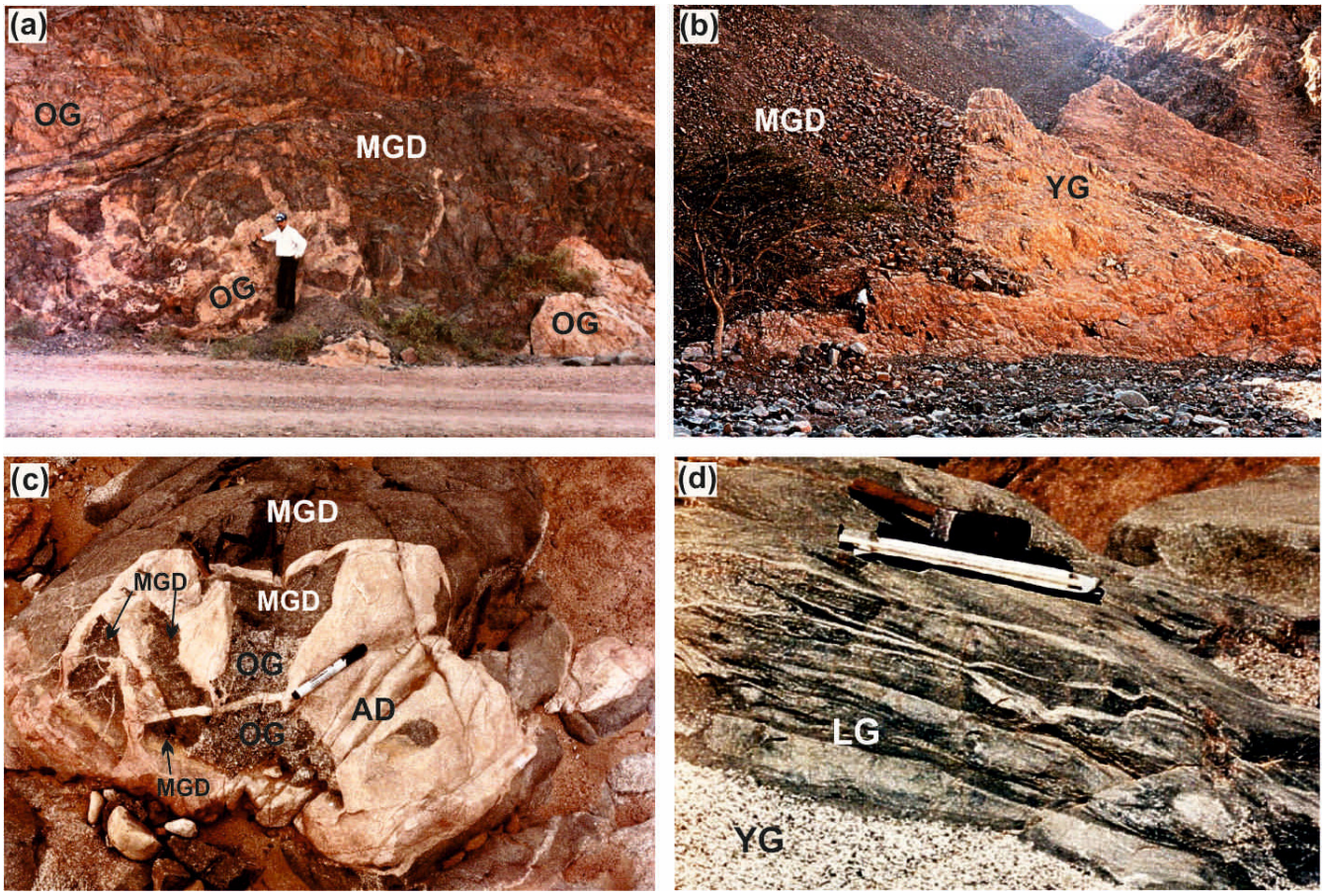


Figure 3. (**a**) Old Granite (OG) intrudes and carries several large xenolithes of metagabbro-diorite rocks (MGD), W. Ba'aba'a. (**b**) Debris-covered contact between Younger Granite (YG) and metagabbro-diorite complex rocks (MGD), W. Samra (looking S 5° E). (**c**) A part of aplitic dyke (AD) cutting metagabbro-diorite rock (MGD) and containing angular xenolithes of it, both isolated and sharply contacted with Old Granite (OG), W. Harqus. (**d**) A part of large boulder showing Younger Granite (YG) intruding layered gabbro (LG) with sharp non-reactive contact, upstream of W. Malhaq.

The Old Granites cover extensive mountainous terrains of moderate relief, particularly in the central part of the area. They are weakly to moderately foliated. Their contact with the metagabbro-diorite complex varies between sharp non-reactivity that displays a variety of shapes and hybridization with reaction zones in between. On the other hand, mafic microgranular enclaves of amphibolite or melanocratic microdiorite are very commonly distributed throughout Old Granite outcrops.

Younger Granites are the most dominant rock unit exposed in the central and southern parts of this area. They exhibit steep-walled, bold mountains with sharp boundaries, locally capped by scattered Paleozoic sandstone outliers resting unconformably above them. They are phaneritic granular rocks of normal granite composition, are leucocratic in appearance, and are absent in mafic enclaves compared with the Old Granites. They have intruded on the Old Granites with sharp, even contacts that are usually characterized by the development of a fine-grained chilled margin.

2.2. Wadi Harqus Area

The Wadi Harqus area is located in the central part of the exposed basement rocks of the southern Sinai. This area is a high mountainous rugged terrain of Precambrian basement rocks dissected by the principal streams W. Harqus, W. El Shiekh, and W. El Akhdar (Figure 2b). The highest topographic features include the mountain summits of Gabal Rahaba (1251 m) and Gabal Tarr (1305 m). Abundant dykes and dyke swarms of different compositions and ages crosscut the different basement units with major trends of NNE and NE. The relative-age succession of the basement rocks exposed in this area comprises the following rock units, arranged from the oldest to the youngest [44]: Metagabbro-diorite complex; Island arc Old Granites; Post-collisional Younger Granites.

W. Harqus Metagabbro-diorite complex rocks (HMGDC) are exposed near the summit of Gabal Tarr and along W. Harqus, where they form two parallel elongated masses extending east-west for a few kilometers, in addition to two smaller irregular and circular masses. They form old roof rocks uplifted and intruded by the Younger Granites at Gabal Tarr and are also intruded by the Old Granites at Wadi El Akhdar. Intensive fracturing and huge debris usually prevent the identification of proper contact between this unit and other rock units. However, a diffused or gradational contact between metagegabbro-diorite complex rocks and the Old Granites is identified downstream of W. El Akhdar. Further, angular xenolithes of sharply contacted old granite and gabbro were also recorded in an aplitic dyke cutting through the metagabbro-diorite rocks at W. Hurkus (Figure 3c). At the exposures of Gabal Tarr, the complex rocks exhibit a pronounced variation from coarse to medium-grained varieties and in composition from gabbro to diorite according to the relative proportion of felsic to mafic minerals.

Old Granites crop out in the northeastern and northwestern corners of this area along the northern banks of W. El Akhdar and W. Harqus. Old granites form moderately elevated mounts and hills with gentle slopes covered by their debris and that of other country rocks and their intruding dykes. They are usually highly altered, weathered, sheared, and friable. They are also characterized by well-developed exfoliation and spheroidal-shaped weathering features. These granites are gray to whitish gray in color, often coarse to medium-grained granular but occasionally porphyritic with pink megacrysts of alkali feldspars. They commonly enclose microgranular mafic enclaves of microgabbro, amphibolite, or melanocratic microdiorite. Such enclaves vary in size from a few centimeters up to one meter across and are usually ovoid, but lenticular, platy, and elliptical forms are not uncommon.

Younger Granites are the major exposed rock unit in this area. They intrude the MGDC rocks with sharp contact at Wadi Harqus, while their contact with the Older Granites varies from sharp to slightly diffused. These rocks are usually equigranular, but sometimes porphyritic, grading in size from coarse to medium-grained. They are a variably mottled pink color with dark mafics, primarily biotite.

2.3. Wadi Malhak Area

The W. Malhak area, encompassing the Shahira metagabbro-diorite complex (SMGDC), lies in the extreme northeastern part of the Kid metamorphic complex (KMC), some 20 km south of Dahab City along the western coast of the Gulf of Aqaba (Figures 1 and 2c). The KMC constitutes a domal structure covering about 600 km^2 that comprises four geotectonic units: the Malhak, Heib, and Umm Zariq formations and the Tarr Complex [12,45–47].

The area is low- to moderate-relief terrain with topographic highs that rarely exceed 800 MASL and is dissected by several structurally-controlled streams. The mapped area comprises an association of variably metamorphosed rock assemblages of orthogneisses, metasediments, and metavolcanics (Malhak Formation) and the Shahira metagabbro-diorite complex extruded by post-collisional Dokhan Volcanics and Younger Granites (Figure 2c).

The Malhak Formation is a volcano-sedimentary succession consisting of sequences of massive to schistose dark gray metavolcanics intercalated and interbedded with fine- to medium-grained metasediments. The metasediments prevail in the mapped exposures of this formation, while the metavolcanic rocks increase progressively southward, though still intercalated with metasediments. The metavolcanics are largely felsic to intermediate with subordinate basic composition, comprising lavas and variably-sized pyroclastics (i.e., lapilli tuff, finely bedded tuffs, lapillistone, and breccia). The lavas are massive, 0.5–4 m thick flows, intermittently associated with pillowed lava bodies. The metasediments are plausibly volcanogenic, derived from the preceding volcanics, and comprise pelites, pebbly graywackes, and conglomerates. Deformation and metamorphism have transformed these lithologies into folded schists and phyllites [48,49]. El-Bialy [48] has concluded that the metasediments of the Malhak Formation are geochemically immature, mostly derived from felsic to intermediate igneous sources, and were formerly deposited in a continental arc setting. K/Ar dating of biotite from schists from the Malhak Formation gave an age of 609 ± 12 Ma [50]. Moghazi et al. [51] determined the maximum depositional U-Pb age of 615 ± 6 Ma inferred from detrital zircons for the Malhak Formation.

Gneissic rocks crop out along the Gulf of Aqaba coast and border other basement rocks on the eastern side of the mapped area. They consist of foliated diorites, granodiorites, and tonalites, with occasional mafic-rich xenoliths. The development of augen structure is evident in some outcrops. These orthogneisses were referred to as the Qenaia Formation by Bentor and Eyal [52] and are considered of intrusive origin [53,54]. Moghazi et al. [53] noticed that the diorite was intrusive into the metasediments and metavolcanics and had the traits of volcanic arc granite, and dated it as 581 ± 11 Ma (whole-rock Rb/Sr isochron age).

The investigated Shahira metagabbro–diorite complex occurs as a single large intrusive body (≈20 km^2) along the northern margin of the KMC. It was recognized as a "Sharira gabbro and diorite complex" by Furnes et al. [46], who described it as a layered gabbroic and dioritic massif of at least 2000 m thick. Recently, the Shahira complex rocks have yielded a U–Pb zircon age of 632 ± 4 Ma [4]. The SMGDC forms a moderate-to-high-relief irregular intrusion elongated NNE. The contact between the Shahira intrusion and the metavolcanics/metasediments of the Malhak Formation, along W. Malhak, is evident and sharp. Apart from fine-grained melagabbro, most plausible, a chilled margin, occurring merely in the western and southern margins of this intrusion along its contacts against the metamorphic rocks of the Malhak Formation, the rocks of SMGDC are medium- to coarse-grained granular, varying in color from dark gray and greenish black (gabbros) to speckled black and white (diorites). The mafic members of SMGDC include both isotropic and layered gabbroic rocks. Layering is infrequently recorded in some outcrops, particularly in the northern part of the intrusion (Figure 3d). The dioritic rocks are less common relative to gabbros and are mainly exposed in the southern segment of the intrusion, close to the contact with the metasediments. Contacts between diorites and gabbros are diffused and hardly recognizable.

The aforementioned three metamorphosed KMC rock units are extruded and intruded by the late Neoproterozoic post-collisional Dokhan Volcanics and Younger Granites, respectively. The Dokhan Volcanics (609 ± 10 Ma; [51]) comprise non-metamorphosed varicolored alternating sequences of porphyritic felsic lava flows of prevailing rhyolite–dacite composition, intercalated with compositionally equivalent pyroclastic layers (commonly ignimbrites) [12]. Younger Granites (~602–612 Ma; [4,51]) represent the ultimate major igneous activity in the region, forming vast expanses of large plutons extending laterally outside the mapped area except from the east. They are differentiated in the field into biotite

monzogranites and leuco-syenogranites with gradational mutual contacts. Furthermore, they vary in texture from granular to porphyritic, with pink alkali feldspar megacrysts.

3. Methodology and Analytical Techniques

A set of fifty-eight representative thin sections of the metagabbro-diorite complex rocks from the three studied areas, G. Shahira (n = 13), W. Harqus (n = 15), and W. Ba'aba'a (n = 9), were prepared and microscopically investigated using a polarizing microscope. Among them, 37 fresh and least altered samples were selected for modal analysis and geochemical study. Modal counting was performed at 800–1000 point counts/sample using a Swift automatic point counter and a mechanical stage.

The 37 rock samples chosen for geochemical investigations were analyzed for their major and most trace element contents by X-ray fluorescence spectrometry (XRF) using a Thermo ARL Advant'XP+ sequential XRF spectrometer and for their rare earth elements together with Cs, Hf, and Ta by the inductively coupled plasma mass spectrometer (ICP-MS; Sciex Elan-250, PerkinElmer, Waltham, MA, USA). The analyses were performed at the Geo-Analytical Laboratory, Washington State University, Pullman, WA, USA. Comprehensive accounts of the techniques for chemical analyses are given by El-Bialy et al. [55]. Additionally, thorough details on sample preparation, analytical procedures, precision, and accuracy are given by Johnson et al. [56] and Knaack et al. [57], also available on the WSU Department of Geology website at https://environment.wsu.edu/facilities/geoanalytical-lab/technical-notes/, access on 26 January 2024). Data processing, plotting, and construction of various diagrams involved using the software GCDkit versions 3.0 and 6.1, PetroGraph v. 2 beta, Corel Draw x5, and Triplot 3.1

4. Petrography

The three investigated metagabbro-diorite complex intrusions can be divided on the basis of modal composition into gabbroic (Figure 4a) and dioritic (Figure 4b) rocks. Dioritic samples are comprised of the three complexes and have the most dominant lithology in the HMGDC (Table 1; Figure 4b). Further, gabbroids are distinguished into pyroxene-hornblende gabbros and hornblende gabbros based on the relative proportions of hornblende and pyroxene, whereas dioritic rocks have been subdivided on the basis of modal quartz contents into diorites and quartz diorites (Table 1). The main petrographic characteristics of each of these four rock types are given below.

Table 1. Modal composition (vol.%) of studied metagabbro-diorite complex rocks.

Sample	Lithology	Qtz	Pl	Kfs	Am	Bt	Px	Ol	Op	Ttn	Total
SHG-2	Px-Hb Gabbro	-	54.15	-	31.50	-	8.52	-	4.69	1.15	100.00
SHG-5	Px-Hb Gabbro	-	54.66	-	27.31	-	9.55	1.63	6.05	0.80	100.00
SHG-12	Px-Hb Gabbro	-	61.18	-	24.50	-	8.20	-	5.26	0.85	100.00
SHG-11	Px-Hb Gabbro	-	54.57	-	27.70	-	10.63	-	6.45	0.65	100.00
SHG-6	Px-Hb Gabbro	-	66.62	-	20.10	-	6.88	-	5.39	1.00	100.00
SHG-18	Px-Hb Gabbro	-	55.00	-	20.25	-	19.65	-	4.77	0.34	100.00
SHG-3	Px-Hb Gabbro	-	54.81	-	30.27	-	8.97	-	5.49	0.47	100.00
SHG-13	Px-Hb Gabbro	-	44.11	-	26.26	-	22.40	0.75	6.27	0.20	100.00
SHG-4	Hb gabbro	0.50	63.44	-	27.55	3.62	-	-	4.18	0.72	100.00
SHG-10	Diorite	2.91	65.00	-	17.05	10.01	-	-	4.34	0.70	100.00
SHG-8	Diorite	3.21	67.71	-	17.06	7.60	-	-	3.78	0.65	100.00
SHG-1	Diorite	2.59	70.94	0.65	16.50	4.65	-	-	4.10	0.57	100.00
SHG-16	Diorite	4.25	66.85	0.35	18.28	6.50	-	-	3.78	-	100.00
Hq5	Px-Hb Gabbro	-	62.87	-	16.55	-	13.25	1.99	5.34	-	100.00
Hq 9	Px-Hb Gabbro	-	58.08	-	27.18	-	8.13	-	5.74	0.86	100.00
Hq11	Px-Hb gabbro	-	65.81	-	20.49	-	8.02	-	5.12	0.55	100.00
Hq1	Hb Gabbro	-	61.77	-	33.54	-	-	-	4.24	0.46	100.00

Table 1. *Cont.*

Sample	Lithology	Qtz	Pl	Kfs	Am	Bt	Px	Ol	Op	Ttn	Total
Hq25	Diorite	2.42	69.90	-	17.03	8.5	-	-	1.68	0.46	100.00
Hq31	Diorite	2.73	70.53	-	17.88	5.3	-	-	3.04	0.52	100.00
Hq12	Diorite	3.99	63.41	-	21.68	6.3	-	-	4.16	0.46	100.00
Hq3	Diorite	4.08	61.60	-	21.81	7.5	-	-	4.54	0.47	100.00
Hq18	Diorite	3.90	69.27	-	11.66	11.8	-	-	3.23	0.14	100.00
Hq20	Diorite	3.33	64.93	-	19.96	7.5	-	-	4.11	0.17	100.00
Hq8	Diorite	2.99	70.86	-	13.29	9.1	-	-	3.76	-	100.00
Hq6	Qz diorite	5.39	59.46	0.54	17.56	13.1	-	-	3.95	-	100.00
Hq10	Qz diorite	5.33	69.65	0.60	10.30	10.9	-	-	3.22	-	100.00
Hq22	Qz diorite	6.27	65.09	0.72	11.36	13.9	-	-	2.19	0.46	100.00
Hq33	Qz diorite	5.72	67.90	0.69	13.80	10.87	-	-	1.02	-	100.00
Ba7	Px-Hb Gabbro	-	73.90	-	15.38	-	7.09	0.46	3.01	0.15	100.00
Ba9	Px-Hb Gabbro	-	64.08	-	22.75	-	7.62	-	5.06	0.49	100.00
Ba8	Px-Hb Gabbro	-	61.08	-	25.66	-	8.99	-	4.06	0.20	100.00
Ba12	Hb gabbro	-	69.70	-	24.70	-	1.10	-	3.98	0.52	100.00
Ba16	Hb gabbro	0.85	62.61	-	29.20	-	2.68	-	4.00	0.66	100.00
Ba5	Hb gabbro	0.98	62.83	-	27.45	-	3.90	-	4.34	0.50	100.00
Ba2	Diorite	3.88	66.84	-	17.20	7.50	-	-	4.05	0.53	100.00
Ba15	Diorite	3.33	61.73	-	20.88	10.52	-	-	3.04	0.50	100.00
Ba11	Qz diorite	5.84	61.52	0.47	12.77	14.20	-	-	4.69	0.51	100.00

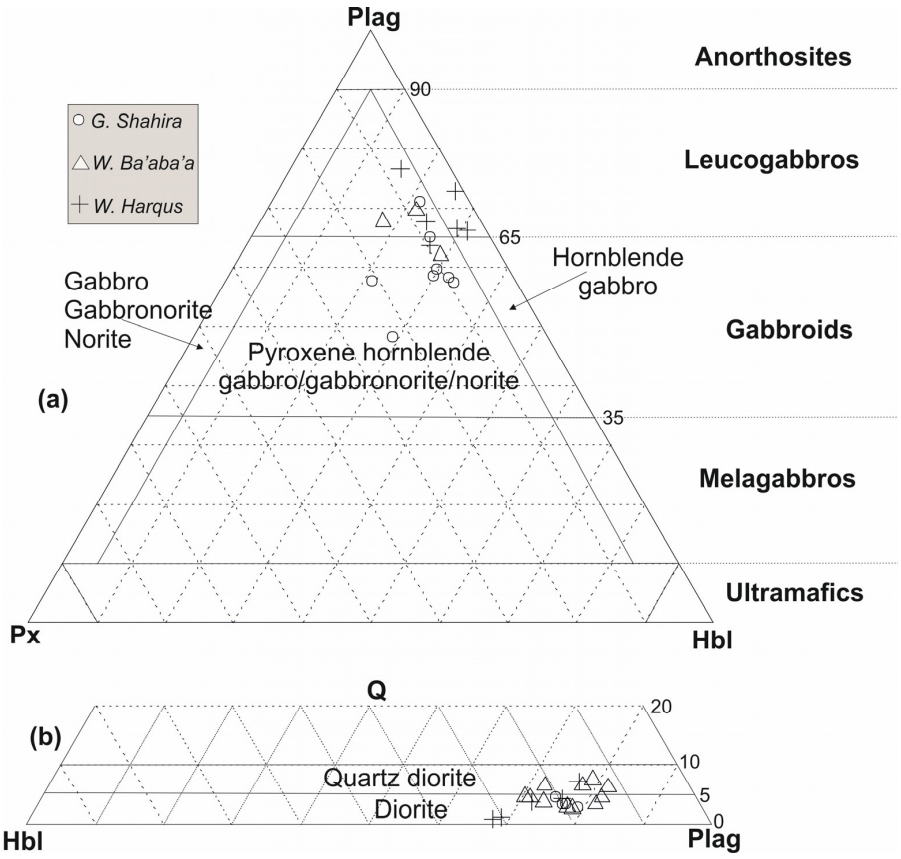


Figure 4. Modal composition of the investigated samples. (**a**) Plagioclase-hornblende-pyroxene diagram [58] for the modal classification of the gabbroids (<1% quartz). (**b**) Quartz-plagioclase-hornblende diagram (after Stern et al., [33]) for the modal classification of diorites (2%–5% quartz) and quartz diorites (>5% quartz).

4.1. Pyroxene-Hornblende Gabbro

The pyroxene-hornblende gabbros predominate relative to hornblende gabbros in the investigated intrusions and in the SMGDC in particular. They are equigranular and melanocratic rocks that vary in absolute granularity from fine to coarse-grained. Although most samples lack olivine, occasional olivine-bearing phases are recorded in the three studied intrusions (Table 1; Figure 5a). The ratio of hornblende to pyroxene varies from about 4:1 to almost 1:1 (Table 1).

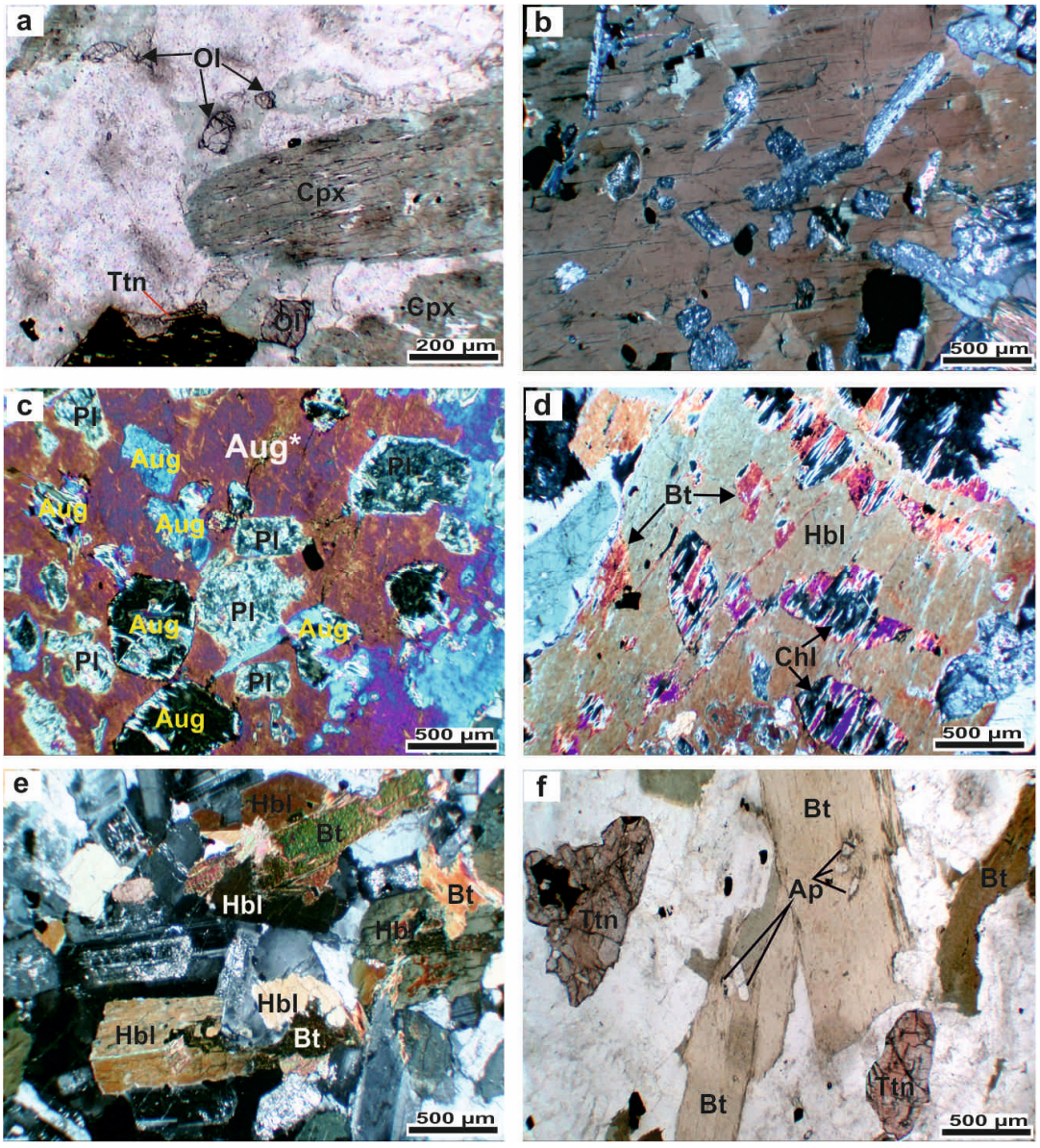


Figure 5. (**a**) Small olivine crystals (Ol) in association with clinopyrpxene (Cpx) and decomposed titanite (Ttn) in pyroxene-hornblende gabbro from SMGDC. (**b**) Part of hornblende oikocryst showing ophitic texture with numerous embedded inclusions of plagioclase laths in pyroxene-hornblende gabbro from HMGDC. (**c**) Early-formed augite (Aug) and sericitized plagioclase (Pl) inclusions enclosed in larger augite crystal (Aug*) in pyroxene-hornblende gabbro from SMGDC. (**d**) Patches of secondary biotite (Bt) and chlorite (Chl) replacing hornblende (Hbl) in hornblende gabbro from BMGDC. (**e**) Mafic coalescences of hornblende (Hbl) and biotite (Bt) in diorite from BMGDC. (**f**) Biotite flakes in association with titanite and encompassing apatite (Ap) inclusions in quartz diorite from HMGDC. All photomicrographs have been taken in crossed polarized light except (**a**,**f**).

The coarse-grained rocks are mainly composed of euhedral plagioclase, anhedral hornblende, subhedral clinopyroxene, and opaques with rare orthopyroxene. Biotite, actinolite, sericite, and chlorite occur as secondary phases, while opaque Fe-Ti oxides, titanite, and apatite are accessory phases. Ophitic and subophitic textures consisting of poikilitic pyroxene and hornblende crystals, including variably resorbed subhedral plagioclase, are commonly observed (Figure 5b). Fine-grained varieties tend to exhibit intergranular texture. Augite in pyroxene-rich samples from SMGDC exhibits a spectacular ophitic texture in which large augite oikocrysts enclose early-formed smaller augite as well as plagioclase (Figure 5c).

Plagioclase occurs as subhedral to anhedral crystals of Bytownite-Labradorite composition ($An_{65–85}$) that occasionally show faint zoning. Plagioclase crystals are seldom fresh and are commonly extensively segregated, particularly along their cores. Pyroxene-hornblende gabbros contain both primary and secondary amphiboles.

The secondary amphiboles comprise actinolite, replacing primary hornblende and clinopyroxene. Clinopyroxenes are mainly represented by augite, which is variably altered to actinolite-tremolite.

4.2. Hornblende Gabbro

The hornblende gabbro is subordinate in SMGDC and HMGDC but, conversely, predominates among the gabbroids of the BMGDC. Hornblende gabbros are either quartz-absent or quartz-bearing (Table 1). The hornblende gabbros exhibit a weakly porphyritic to equigranular texture and consist of euhedral to subhedral plagioclase and hornblende crystals, plus or minus subordinate interstitial quartz, biotite, and augite, with titanite, magnetite, and apatite as accessories. In the weakly porphyritic variety, larger plagioclase megacrysts (>5 mm) have a higher anorthite content (only bytownite) and are less susceptible to alteration relative to the later crystallized smaller plagioclase ($An_{75–60}$). Hornblende commonly occurs as poikilitic large crystals, which are up to 10 mm long, embracing plagioclase laths and occasional opaques. Whenever present, augite mostly occurs as relicts in hornblende. Patches of secondary biotite and chlorite replacing hornblende are rather common (Figure 5d).

4.3. Diorite and Quartz-Diorite

Diorite and quartz diorite constitute integral parts of the three investigated metagabbro-diorite complexes (Figure 4b). They are phaneritic rocks of fine- to medium-grained hypydiomorphic granular and seriate textures, consisting essentially of, plagiocalse, mafics, and interstitial quartz, along with insignificant alkali feldspars. Mafics are represented by both biotite and hornblende in broadly different relative proportions, although hornblende always predominates (Figure 5e). Plagioclase is euhedral to subhedral prismatic and equant andesine-labradorite ($An_{35–55}$). Twining in plagioclase crystals may be obscured by chemical zoning, either normal or oscillatory, or pervasive sericitization. The sericitization may be uniform or concentrated, either in the core or in submarginal concentric zones. Quartz occurs as relatively small interstitial grains that seldom exceed 1 mm in diameter. It occasionally contains tiny relics of plagioclase and mafics and varies in extinction from even to mild wavy and undulatory. Alkali feldspars are of limited abundance (<1%) or almost absent in some samples and are represented by sparse small anhedral microperthite and cryptoperthite that occur interstitial to other constituents.

Biotite forms tabular and platy crystals with rugged boundaries and occasional corroded insides on account of the invasion of later-formed plagioclase and quartz. It is pleochroic in shades of yellow, green, and brown. Biotite crystals occur either individually or coalesce in assemblages of sticked flakes. Secondary, patchy biotite formed at the expense of hornblende is not uncommon. Biotite is often sieved by apatite inclusions and is closely associated with titanite (Figure 5f). Minute metamict zircon inclusions are occasionally observed in some biotite.

Hornblende commonly occurs as pleochroic green euhedral to subhedral prismatic crystals of pseudohexagonal cross sections, or less commonly as smaller, resorbed, ill-defined-shaped grains. The former crystals occasionally display simple twinning (Figure 5e). Hornblende sometimes forms aggregates of bunched crystals either solely or in participation with biotite (Figure 5e).

5. Geochemistry

Whole-rock major, trace, and REE element data of the investigated three metagabbro-diorite complexes in Sinai are listed in Supplementary Materials Tables S1 and S2, along with calculated normative compositions, various geochemical ratios, and parameters, in addition to apatite and zircon crystallization temperature estimates. Table 2 presents a comparison between the average geochemical data of the three studied complexes and other published averages of metagabbro-diorite complexes, mostly from the Egyptian Eastern Desert.

5.1. Major Elements and Classification

Plotting of the studied MGDC samples on the total alkalis-silica (TAS) diagram for plutonic rocks of Middlemost [59] reveals that they mainly straddle the gabbro, gabbroic diorite, and diorite fields, with occasional samples classified as monzogabbro, monzodiorite, monzonite, quartz monzonite, and granodiorite (Figure 6a). The use of the recent normative 2Q-(Or+Ab)-4An diagram proposed by Enrique [60] has a quite similar outcome, as most samples are classified as gabbros, diorites, quartz gabbros, and quartz diorites (Figure 6b). The results of both geochemical classifications closely approximate the modal classification of the studied MGDC rocks (Figure 6b). The studied MGDC rock samples span the discriminating boundary between subalkaline alkaline and magma series of Miyashiro [61] on the TAS diagram with significant bias towards the subalkaline field (30 out of 37 samples) (Figure 6a). Plotting of the former 30 subalkaline samples on the AFM diagram [62] shows that they possess a prevalent calc-alkaline character over a subsidiary tholeiitic one. The mild alkaline affinity of some samples (n = 7) from G. Shahira and W. Hurqus MGDCs is not inimitable and has been previously reported for Shahira MGDC [36]. Otherwise, all the published works on the Egyptian MGDCs from the Eastern Desert and Sinai are predominantly calc-alkaline to slightly tholeiitic (e.g., [29,30,33–35]). Regarding alumina saturation, Table S1 reveals that, apart from three peraluminous samples (A/CNK > 1) from W. Harqus, the studied MGDC rocks are metaluminous with A/CNK < 1 and A/NK > 1 and usually have normative titanite ± diopside and lack normative corundum. Once again, the metaluminous to slightly peraluminous nature is common among other Egyptian MGDCs (e.g., [29,32,34]). Among the studied samples, a primitive gabbroic sample from each of the investigated MGDCs is silica-undersaturated, lacking normative quartz, and nepheline- and/or olivine-normative (Table S1).

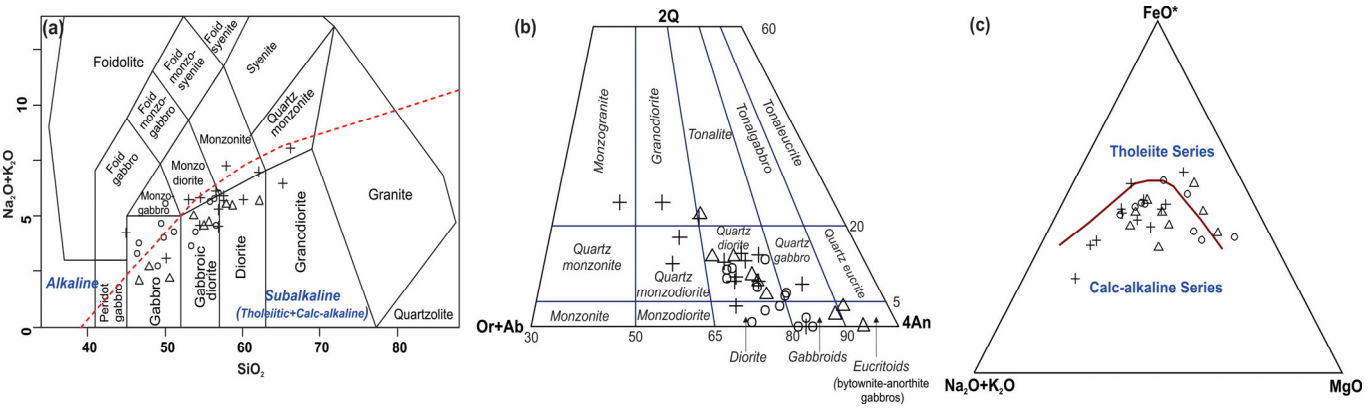


Figure 6. Classification of the three studied MGDC rocks using: (**a**) Total alkalis vs. silica (TAS) diagram of Middlemost [58], with the alkaline-subalkaline discriminating line after Miyashiro [61]. (**b**) CIPW-normative triangular diagram 2Q-(or + ab)-4an-2F for the classification of plutonic rocks (after Enrique, [59]). (**c**) AFM diagram for the distinction between tholeiitic and calc-alkaline samples [61]. Symbols as in Figure 4.

Compared to other Egyptian MGDCs (Table 2), the studied MGDCs are moderately evolved suites of wide compositional variations, with their SiO_2 contents ranging from ca. 44 wt.% for the most basic varieties in the three studied complexes up to around 63 wt.% in the most evolved quartz diorites (Table S1). Correspondingly, all the major oxides show very varied ranges; for instance, Al_2O_3: 12.77–24.47 wt.%, FeO*: 3.48–13.29 wt.%, MgO: 1.69–9.05 wt.%, CaO: 2.58–13.11 wt.%, Na_2O: 1.52–5.03 wt.%, and K_2O: 0.21–3.23 wt.%. These wide major oxide ranges are more or less continuous except for alumina, which shows a considerable compositional gap between 19.43 wt.% and 24.47 wt.%. Furthermore, their differentiation indices (DI, sum of normative Q + Or + Ab: [63]) and Mg-numbers (Mg# = Mg/(FeO + MgO)) broadly fluctuate between a minimum of 31.66 and 34.45 and a maximum of 79.99 and 70.37, respectively (Table S1).

Table 2. Comparison of average Whole-rock major (wt.%), trace, and rare earth element (ppm) concentrations of the three investigated metagabbro-diorite complexes with others from Sinai and North, Central, and Southern Eastern Desert segments (NED, CED, and SED, respectively.

Reference	**This Study**				**1**	**2**	**3**	**4**	**5**	**6**	**Average**
Locality	**G.**	**W.**	**W.**	**All**	**Sinai**	**NED**	**CED**		**SED**		**Cont.**
	Shahira	**Harqus**	**Ba'aba'a**	**Samples**	**Shahira**	**Um Balad**	**W. El-Markh**	**G. Atud**	**Um Eleiga**	**Rahaba**	**Crust**
No. of Samples	13	15	9	37	15	18	16	10	30	30	-
SiO_2	50.14	54.88	52.40	52.61	49.77	57.38	58.09	48.74	55.94	57.88	60.60
TiO_2	1.23	0.99	0.88	1.05	1.04	0.63	0.80	0.65	0.71	0.70	0.72
Al_2O_3	16.28	17.20	18.24	17.13	18.04	17.33	16.64	19.14	16.57	17.26	15.90
FeO*	9.80	7.71	7.21	8.32	8.97	8.46	6.12	6.22	8.85	6.62	6.71
MnO	0.15	0.11	0.11	0.12	0.13	0.12	0.11	0.10	0.20	0.14	0.10
MgO	6.08	3.68	4.97	4.84	5.96	3.52	5.19	8.36	4.77	3.76	4.66
CaO	8.25	6.11	8.53	7.45	9.19	5.14	7.33	13.00	5.95	5.86	6.41
Na_2O	2.90	3.69	3.21	3.30	2.45	2.77	3.48	2.08	3.01	3.37	3.07
K_2O	1.41	1.77	0.82	1.41	1.12	1.55	1.24	0.24	1.59	1.87	1.81

Table 2. *Cont.*

Reference	This Study				1	2	3	4	5	6	Average
Locality	G. Shahira	W. Harqus	W. Ba'aba'a	All Samples	Sinai Shahira	NED Um Balad	CED W. El-Markh	CED G. Atud	SED Um Eleiga	SED Rahaba	Cont. Crust
P_2O_5	0.23	0.30	0.23	0.26	0.31	0.18	0.17	0.05	0.59	0.17	0.13
LOI	2.06	2.23	1.97	2.11	2.18	2.99	0.71	2.04	1.75	1.39	-
Total	98.52	98.67	98.57	98.59	99.15	100.16	99.88	100.71	99.93	99.00	100.12
Ni	57.14	52.09	46.00	52.38	44.64	17.11	53.44	49.86	27.30	76.95	59.00
Cr	115.63	88.64	111.70	103.73	105.71	26.47	238.31	408.00	127.87	175.72	135.00
Sc	26.74	3.17	21.41	15.89	26.43	18.28	26.50	28.29	-	16.09	21.90
V	247.97	154.07	158.67	188.18	188.29	162.61	140.25	155.90	112.43	152.20	138.00
Cs	1.89	2.00	1.66	1.88	0.79	1.91	-	0.29	-	-	2.00
Ba	358.84	597.61	346.27	452.58	267.36	362.03	282.75	70.03	827.00	365.52	456.00
Rb	39.53	53.42	25.93	41.86	27.21	53.67	42.69	4.19	42.30	20.05	49.00
Sr	674.03	674.62	763.87	696.12	699.21	453.77	497.63	370.90	602.40	323.45	320.00
Hf	2.61	2.71	2.42	2.61	2.36	2.09	2.57	0.99	-	2.51	3.70
Zr	85.79	177.62	96.50	125.62	84.36	77.50	108.75	35.00	168.43	115.12	132.00
Y	17.81	28.15	12.04	20.60	17.43	14.86	20.88	9.76	22.38	14.65	19.00
Ta	0.30	0.02	0.30	0.19	0.31	3.35	-	0.07	-	0.24	0.70
Nb	4.79	5.60	5.13	5.20	3.57	0.33	2.63	0.98	13.20	3.64	8.00
Ga	19.01	45.09	23.31	30.63	-	-	-	14.33	-	9.52	16.00
Cu	45.95	46.44	34.07	43.26	46.07	-	34.00	30.34	20.53	-	27.00
Zn	96.77	107.87	80.95	97.42	92.00	-	61.25	41.78	66.40	78.96	72.00
Pb	5.23	12.22	15.77	10.63	20.50	21.92	9.69	1.44	-	6.45	11.00
Th	2.53	2.22	2.45	2.39	1.71	2.09	16.38	0.34	-	1.66	5.60
U	1.27	0.99	0.54	0.98	1.15	1.62	1.46 1.96	0.14	-	0.63	1.30
La	14.76	20.31	17.37	17.64	12.95	14.47	13.50	2.82	10.37	17.67	20.00
Ce	32.20	37.69	31.27	34.20	31.25	26.15	29.38	6.83	20.79	40.55	43.00
Pr	4.12	5.28	3.34	4.40	4.15	3.02	-	0.98	-	5.25	4.90
Nd	19.19	24.93	15.92	20.72	18.10	12.26	19.63	4.77	11.19	22.61	20.00
Sm	5.17	4.25	3.83	4.47	4.48	2.46	-	1.48	2.71	6.04	3.90
Eu	1.63	1.38	1.17	1.42	1.20	0.87	-	0.63	0.86	1.92	1.10
Gd	4.73	5.07	4.40	4.79	3.52	2.62	-	1.66	2.30	5.91	3.70
Tb	0.73	0.79	0.68	0.74	0.56	0.39	-	0.28	0.32	0.92	0.60
Dy	4.30	2.53	2.35	3.11	3.47	2.47	-	1.80	-	5.50	3.60
Ho	0.82	0.49	0.45	0.60	0.67	0.52	-	0.37	-	1.13	0.77
Er	2.12	2.14	1.88	2.07	1.87	1.65	-	1.06	0.96	3.05	2.10
Tm	0.29	0.29	0.26	0.28	0.26	0.22	-	0.15	-	0.43	0.28
Yb	1.73	1.21	1.30	1.41	1.60	1.51	-	0.97	0.92	2.45	1.90
Lu	0.26	0.16	0.23	0.21	0.22	0.23	-	0.14	0.12	0.36	0.30
ΣREE	92.04	106.52	84.44	96.07	84.31	68.84	62.50	23.93	50.55	113.80	106.15

References: 1- [36]; 2- [35]; 3- [30]; 4- [33]; 5- [29]; 6- [34]. *Average composition of the continental crust is after Rudnick and Gao* [64].

On the Harker variation diagrams, the studied samples represent a continuous wide spectrum of compositions (SiO_2: 44.1–63.22 wt.%) with no marked silica gap (Figure 7a). Excluding the alkalies Na_2O and K_2O plus P_2O_5 showing variably positive trends, other major oxides display progressive decline against silica rise. Whether positive or negative, the tendencies vary from markedly rectilinear (e.g., FeO* and CaO) to highly scattered (e.g., Al_2O_3 and P_2O_5). These major oxide trends are in harmony with fractional crystallization, since Al_2O_3, CaO, MgO, FeO*, and TiO_2 fall owing to plagioclase, pyroxene amphiboles, and Fe-Ti oxide fractionation with differentiation.

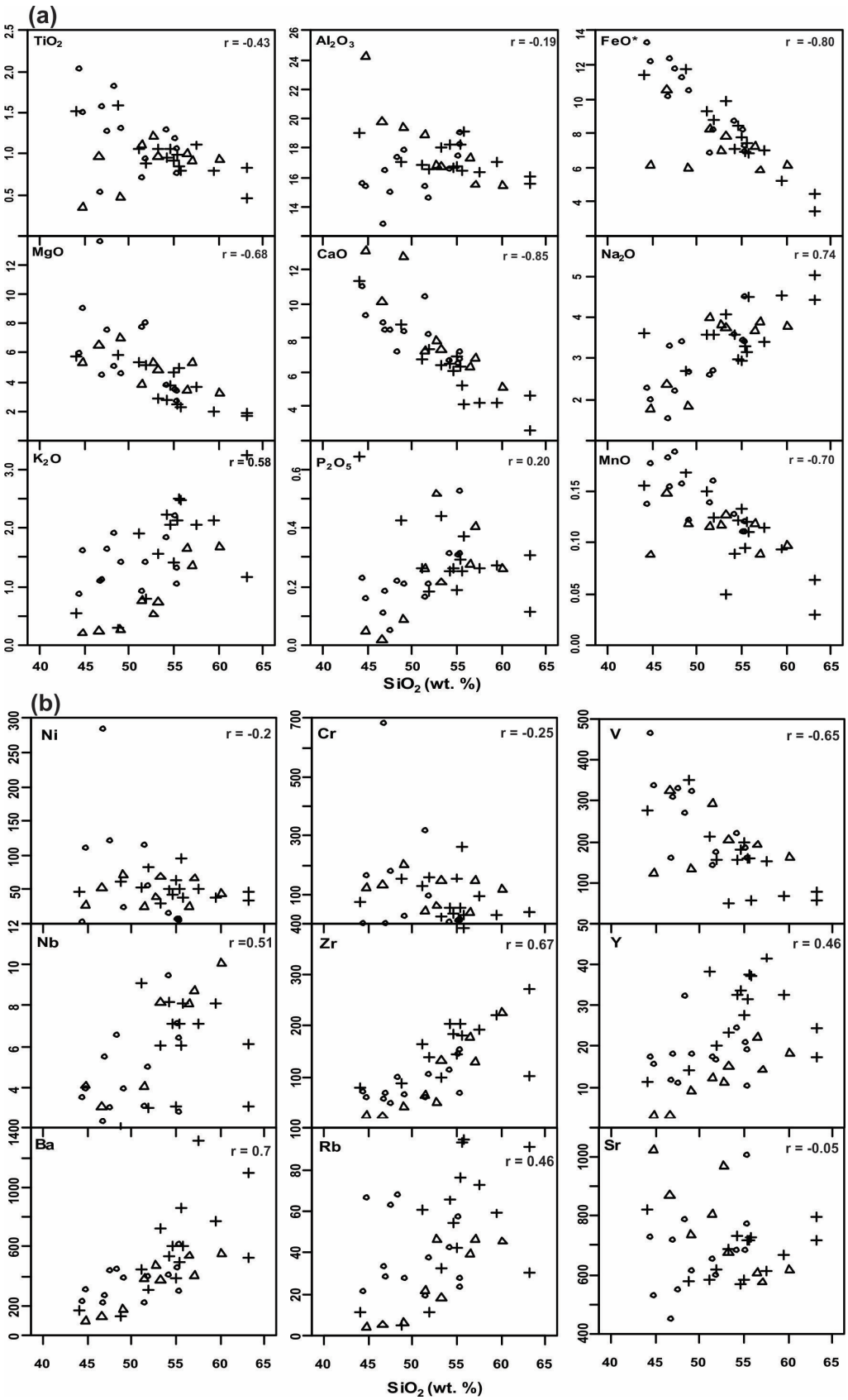


Figure 7. Harker-type variation diagrams for the studied MGDCs: (**a**) Major oxides (wt.%). (**b**) Selected trace elements (ppm). Symbols as in Figure 4.

5.2. Trace Elements

Table 2 reveals that the averages of almost all trace element abundances in the investigated samples are more or less comparable with those of other Egyptian metagabbro-diorite complexes. However, among the studied MGDCs, G. Shahira MGDC samples exhibit higher abundances and averages of the compatible transition metals Ni (average = 57.14 ppm), Cr (average = 115.63 ppm), Sc (average = 26.74 ppm), and V (average = 247.97 ppm) compared with those of W. Ba'aba'a and W. Harqus (Table 2 and Table S2). On the other hand, they possess lower abundances and averages in the high-field strength elements (HFSE) Zr (average = 85.79 ppm) and Nb (average = 4.79 ppm). Noteworthy, the investigated metagabbro-diorite rocks have remarkably low Nb contents (average of all samples = 4.79 ppm), which is typical of magmatic rocks evolved in arc-type settings.

Harker multi-trace element diagrams of the studied MGDC samples show slightly dispersed positive and negative trends (Figure 7b). The degree of scatter is more evident for Ni, Cr, and Sr (r = −0.2, −0.25, and −0.05, respectively) against silica rise. Other plotted trace elements show more tight semi-linear trends (e.g., Ba and Zr; r = 0.7 and 0.67, respectively). Generally, the ferromagnesian compatible trace elements Ni, Cr, and V, along with Sr, being compatible with Ca-plagioclase, show negative trends typified by general regression with differentiation (increase in SiO_2), whereas other incompatible LILE (e.g., Ba and Rb) and HFSE (Zr, Nb, and Y) reversely exhibit elevations (Figure 7b). The general narrow scatter and fair linear trends in trace element Harker diagrams imply a possible role of magma mixing, as it is supposed to be the conventional source of linear trends in Harker diagrams (c.f., [64,65]).

Table S2 reveals that the analyzed MGDC rocks possess a limited range of very low Rb/Sr ratios (0.01–0.13) with an average of 0.06. The vast majority of the calculated Rb/Sr values are utterly lower than the upper and middle continental crust values (0.26 and 0.23, respectively), but bestride the lower continental crust value (0.03) [66].

Apart from one bizarre hornblende gabbro sample from W. Ba'aba'a with a very low K/Rb ratio (93), most of the studied samples show K/Rb values (203–568; average = 317) higher than those of average for igneous rocks (230; [67]) and the chondritic values (242; [67]), too (Table S2). Moreover, these K/Rb values are indicative of the dominance of crystal–melt equilibria since they are greater than 160 [68], the absence of post-magmatic aqueous fluid interactions, and/or mineral crystallization induced by aqueous fluids, which characteristically give rise to K/Rb ratios less than 100 [69,70].

Almost all of the available Zr/Hf ratios of the analyzed samples (31.08–58.65, average = 36.7; Table S2) center around the chondritic values (36.6 and 34.3, respectively [71,72]), continental crust (Zr/Hf = 33; [73]), and the limited range (33–40) characterizing most magmatic rocks [74]. However, many of them (13 out of 31) surpass the chondritic values (>36), are comparable to those of OIB and E-MORB (34–42; [75]), and approach the depleted mantle Zr/Hf values (35.7–45.53; [76]).

Determined Y/Nb ratios show considerable variations between the three investigated MGDCs and even between samples within each complex (Table S2). The Y/Nb values fluctuate between the ranges of 2.92–5.07 (av. = 3.96 for G. Shahira samples), 2.83–8.71 (av. = 5.21) for W. Harqus samples, and 0.75–3 (av. = 2.03) for W. Ba'aba'a samples. This ratio has been assumed to be fundamental in recognizing magma sources, as igneous rocks derived from mantle sources possess Y/Nb ratios below 1.2, whereas crustal-derived ones are typified by Y/Nb ratios greater than 1.2 [77].

The mantle-derived magmas have almost constant near-chondritic Nb/Ta ratios of 17.6 [72,78–82]. Conversely, Nb/Ta ratios of continental crust, which is supposed to be differentiated from mantle-derived magmas in subduction zones, are markedly lower and subchondritic (~11–13; [68,73,82–84]), implying that the pair Nb and Ta were fractionated from each other in the continental crust. Although the Nb/Ta ratios of the studied three MGDC samples show quite variation (10.81–18.73), they maintain comparable subchondritic averages (=15.93, 13.34, and 13.48; Table S2).

N-MORB-normalized incompatible multi-element spider diagrams [85] of the three investigated MGDCs show evident comparability and overlap (Figure 8). Obviously, the three MGDCs display evidently similar patterns of rather steep slope with noticeable tilting of the profiles up to left due to preferential enrichment of the incompatible elements at the left-side of the diagram (i.e., LILE, HFSE, and LREE) over the more compatible elements to the right (i.e., MREE, Ti, Y, and HREE) (Figure 8). In addition, the most distinctive and mutual features in the profiles of the investigated MGDCs are the distinctly deep negative Nb anomalies and the projecting positive Pb spikes. Further, almost all of the patterns exhibit slight positive projections at Ba, K, Sr, and Nd. The most patent depletions are shown by Ti, MREE, Y, and HREE, with concentrations even below those of N-MORB.

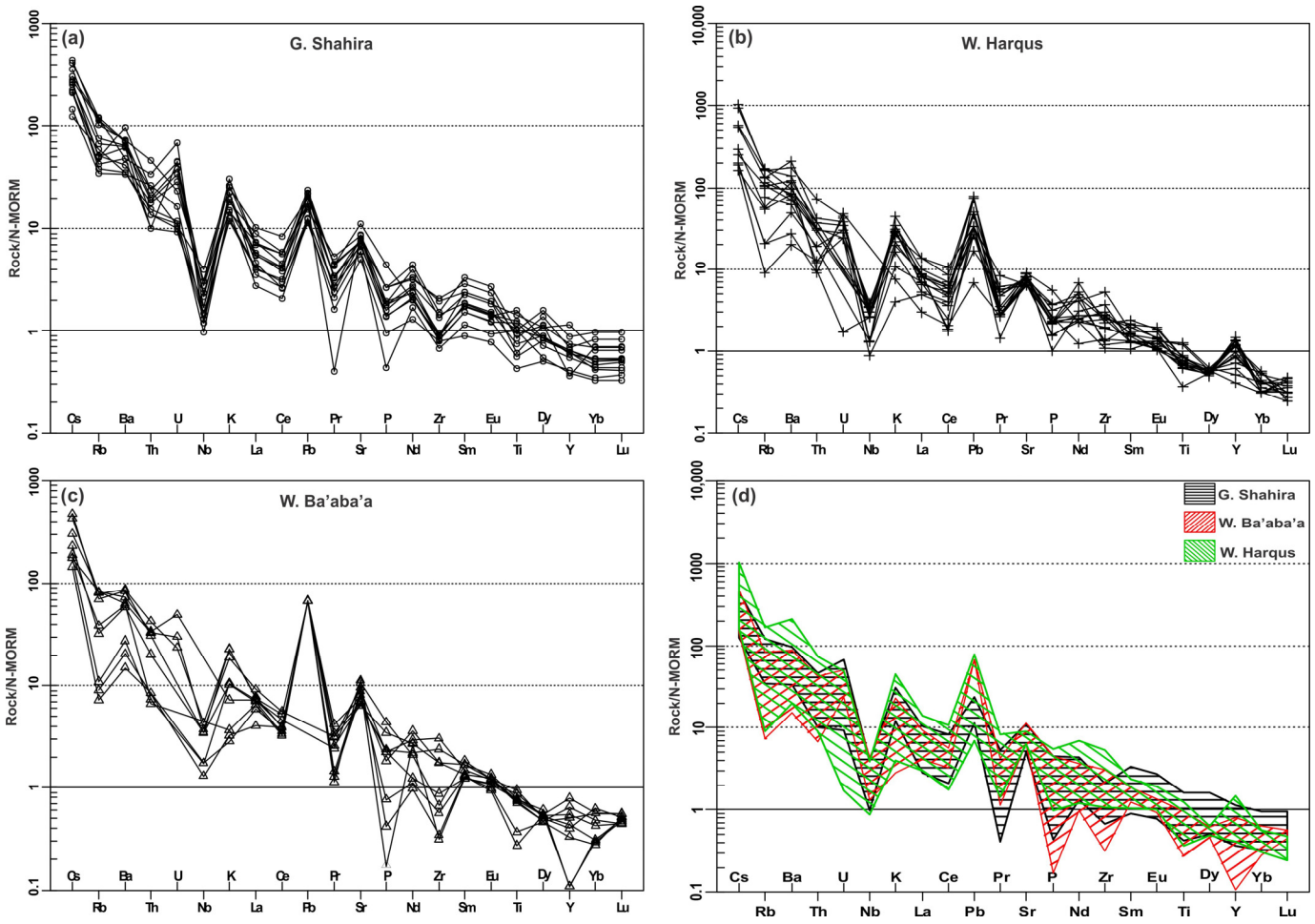


Figure 8. N-MORB-normalized multi-element spider diagrams for the studied MGDCs. N-MORB values are from Sun and McDonough [84]. (**a**) G. Shahira; (**b**) W. Harqus; (**c**) W. Ba'aba'a; (**d**) Combined fields of the three areas. Symbols as in Figure 4.

The coincidence of stout negative Nb and positive Pb anomalies on MORB and primitive mantle spider diagrams is typical of igneous rocks evolved in subduction zones and definitely denotes incorporation of crustal material (C.f., [86–90]) and is frequently recorded in other MGDCs in the Eastern Desert (e.g., [30,33,42]). The fluid-mobile LILEs Cs, Rb, and Ba relative enrichment (10–1000 × MORB) insinuates the contribution of fluids released from the subducted slab since they are the most mobile and rich elements in such fluids [90–92]. The extensive depletions in Zr, Ti, and P are presumably attributed to the fractionation of zircon, illmenite, titanomagnetite, and apatite, respectively. Nonetheless, the substantial depletion of these elements in the studied MGDC rocks, which is sometimes

below their abundance in MORB (Figure 8c), necessitates a progressive fractionation of such minerals at upper crustal levels.

5.3. Rare Earth Elements

The rare earth element concentrations of the thirty-seven studied MGDC samples, along with their total REE contents, the Eu anomaly measure (Eu/Eu*), and some substantial C1-chondrite-normalized ratios, are listed in Table S2.

Although the samples from the three MGDCs exhibit variably LREE-enriched patterns [$(La/Yb)_N$ = 4.92–18.55; av. = 9.04], the samples of G. Shahira show almost parallel smooth patterns, in opposition to the subparallel kinked patterns with alternative Gd-Tb and Er-Tm plateaus and a Dy-Ho trough in between for the W. Ba'aba'a and W. Harqus samples (Figure 9). Likewise, G. Shahira REE patterns lack Eu anomalies (Eu/Eu* ≈ 1), while the other two MGDCs show negligible and weak positive and negative Eu anomalies.

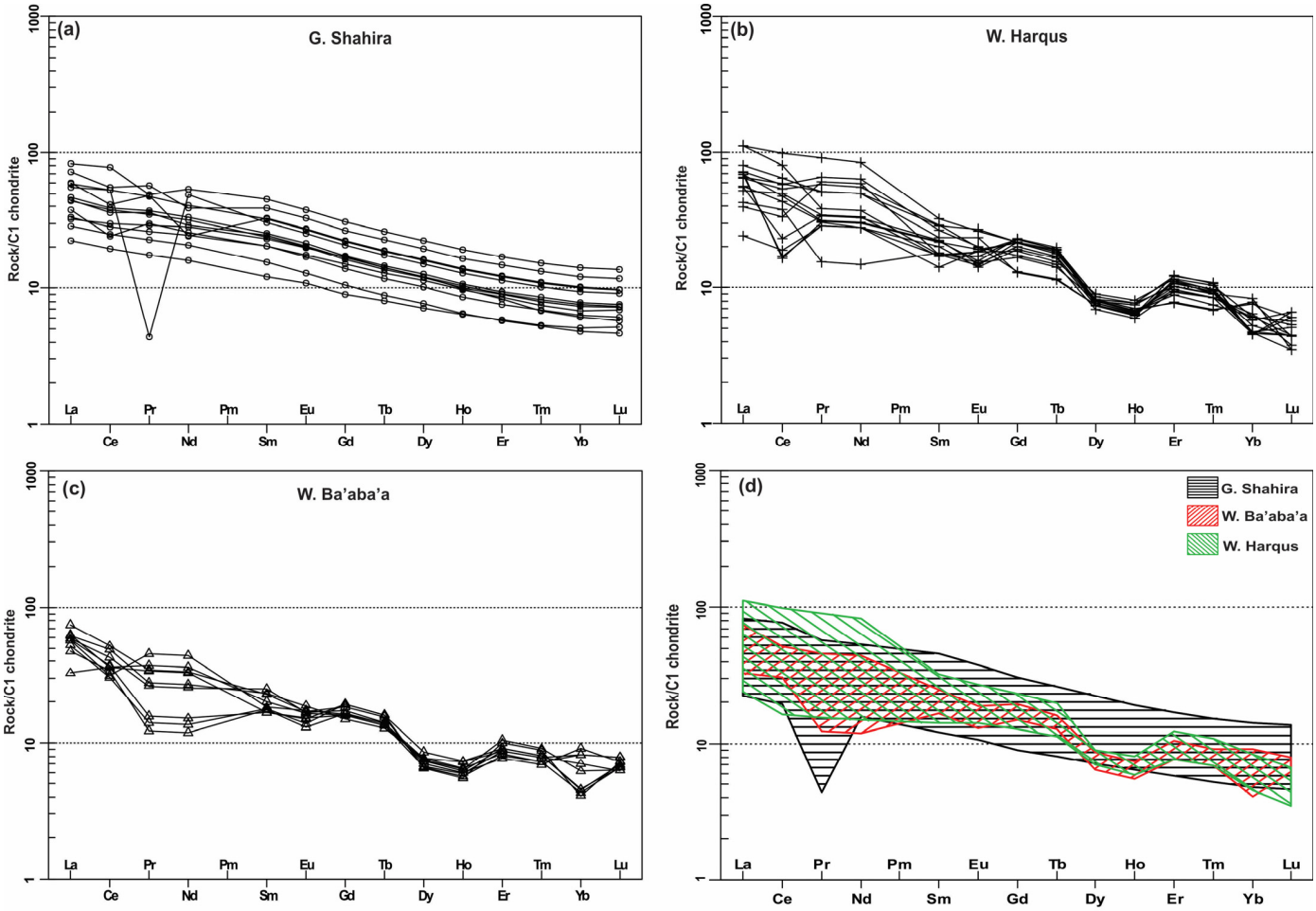


Figure 9. REE patterns normalized to chondrite [92] for the three studied MGDC rock samples. (**a**) G. Shahira; (**b**) W. Harqus; (**c**) W. Ba'aba'a; (**d**) Combined fields of the three areas. Symbols as in Figure 4.

Samples of W. Harqus complex exhibit the highest degree of REE fractionation [average $(La/Yb)_N$ = 11.7], followed by those of W. Ba'aba'a [average $(La/Yb)_N$ = 9.46], whereas G. Shahira MGDC samples retain the lowest degree of REE fractionation [$(La/Yb)_N$ = 5.69]. The three studied MGDCs possess moderate total REE contents (average 96 ppm for all samples), although they show considerable variations within each complex, viz., G. Shahira (∑REE = 45–163 ppm; av. = 92 ppm), W. Harqus ((∑REE = 60–144 ppm; av. = 107 ppm), and W. Ba'aba'a (∑REE = 66–107 ppm; av. = 84 ppm).

For the whole studied samples, La concentrations fluctuate between nearly 22 and 111 times the chondrite value, while Lu ranges between 4× and 12× chondritic abundances, demonstrating their variably LREE-enriched patterns. The degree of LREE fractionation is modest with gentle slope patterns [$(La/Sm)_N$ = 1.41–6.41; av. = 2.56)], while the heavy REE are more fractionated with slightly steeper patterns [$(Gd/Yb)_N$ = 1.77–4.91; av. = 2.92]. For all samples, and those from G. Shahira MGDC in particular, the HREE (Ho-Lu) is not depleted (≈5–20 times chondrite values), and is further comparable to the middle REE, denoting the absence of garnet in the crustal source or its accumulation in the refractory residue through partial melting, since HREE is exceedingly compatible with garnet [91].

All the REE patterns of the studied Shahira MGC samples lack or possess negligible Eu anomalies (Eu/Eu* = 0.95–1.05), while those of W. Harqus samples exhibit both negligible and delicate negative Eu anomalies, and those of W. Ba'aba'a samples have both marked negative and occasional positive (3 out of 12) Eu anomalies (Table S2). The existence of an Eu anomaly, whether negative or positive, presents an indication of the rule of feldspar in petrogenesis. Negative Eu anomalies are primarily linked to feldspar fractionation, as Eu is strongly compatible with plagioclase and alkali feldspars. Accordingly, the negative Eu anomalies are commonly assigned to the removal of feldspar by crystal fractionation from the melt or the feldspar retention in the source following partial melting. The positive Eu anomalies are unanimously ascribed to feldspar accumulation, whether by segregation from a greater volume of porphyritic magma, rain of liquid from a mush, or assimilation of feldspar-rich rocks. The combination of positive and negative Eu anomalies in the W. Ba'aba'a diorite and quartz diorite samples (Table S2) may be produced by hornblende fractionation, since even though REE is compatible with hornblende in intermediate magmas, Eu has a particularly lower partition coefficient relative to most middle and heavy REE [93,94].

6. Discussion

6.1. Post-Magmatic Alteration

Since there is a consensus that the Egyptian metagabbro-diorite complexes have suffered low-grade metamorphism (up to greenschist or lower amphibolite facies), and some of the petrogenetically critical analyzed major and trace elements (e.g., Ca, Na, K, Sr, Mg, Ba, Rb, Cs, and Pb) are mobile during weathering and hydrothermal alteration, we have examined the degree of plausible alteration that the investigated samples might be subjected to. The occasional occurrence of secondary phases (e.g., sericite, actinolite, and chlorite) formed at the expense of primary plagioclase and ferromagnesian minerals point to an inevitable but slight alteration (Section 3).

The limited range of low loss on ignition (LOI) values (1.27–2.74 wt.%; average = 2.11 wt.%) among the analyzed samples indicate that they have not been considerably affected by alteration. The narrow scatter of the more mobile LILE Na, K, Rb, Ba, and Sr, which appear to be the most affected by hydrothermal alteration, on Harker diagrams (Figure 7) suggests that post-magmatic alteration did not have a significant impact on the whole-rock geochemistry of the investigated samples.

Heavy rare earth elements (HREEs; Gd, Tb, Dy, Ho, Er, Tm, Yb, Lu) are mainly less affected by alteration compared with the LREEs (La, Ce, Pr, Nd, Sm, Eu), which are susceptible to mobilization during post-magmatic alteration [95–98]. Apart from 3 samples from W. Harqus MGCD showing delicate negative Ce anomalies, the rest of the analyzed samples lack Ce anomalies (Figure 9), confirming the limited LREE mobility. In addition, the low values of the LREE/HREE ratio of the studied samples (3.41–11.26; average = 6.27) confirm their minimal alteration since least altered and altered rocks have mean LREE/HREE ratios of ~6.7 and ~17, respectively [95].

The ratio of Y/Ho can be used to assess the degree of alteration (e.g., [99–102]). Conventionally, unaltered magmatic rocks should have a narrow range of Y/Ho close to the chondritic value (24–34; [103]), whereas hydrothermal alteration causes elevation of this ratio up to 44–47 [103,104]. Table S2 reveals that the vast majority of the studied

samples fall within the chondrite range, with an average Y/Ho for all samples of 26.11, which negates the significant rule of hydrothermal alteration in the studied rock samples. Similarly, the Zr/Hf ratio is a sensitive indicator of magmatic-hydrothermal transitional systems [71,73,103]. Most igneous rocks possess Zr/Hf ratios within the range of 26–46, including the values of chondrites (36.6 ± 2.9), while Zr/Hf ratios deviate towards lower values (Zr/Hf < 20) under the influence of hydrothermal alteration [69,103]. With no exception, all our samples have Zr/Hf ratios that vary between 26.8 and 46.39 within an average of 37.12, signifying a lack of significant subjection to post-magmatic alterations (Table S2).

Finally, to quantify the intensity of sericite and chlorite alteration intermittently recorded in the studied MGDC rocks, we calculated the Alteration Index (AI) of Ishikawa et al. [105] for all samples (Table S1). This index was formulated to compare the major rock-forming elements gained ($MgO + K_2O$) against the elements lost and gained ($Na_2O + CaO + MgO + K_2O$) through chlorite and sericite alteration [106]. For unaltered rocks, the index varies from 20 to 60, while values between 50 and 100 pertain to hydrothermally altered rocks, with AI = 100 denoting complete alteration to sericite and/or chlorite. The calculated AI values for the studied samples range between 22.83 and 58.41, with an average of 36.78, confirming that they are least altered.

6.2. Accessory Mineral Crystallization Temperatures

Even though they commonly constitute not more than 1 vol.% of a rock sample, the accessory minerals zircon, apatite, monazite, and rutile host considerable fractions of its trace element budget. Consequently, these accessory mineral phases have been extensively studied in natural and experimental systems to attain empirical models for the calculation of their saturation temperatures (e.g., [107–113]). The geothermometers of zircon, apatite, rutile, and monazite are based on the postulation that the abundances of Zr, P, Ti, and LREE, respectively, in igneous rocks are controlled by the solubility of these accessories in the magma, which is a function of temperature [114–118]. Among these whole-rock-based geothermometers, the rutile and monazite ones are excluded from our investigations as our studied rock samples lack a modal abundance of them. Herein, we calculated two independent magmatic saturation temperatures using zircon and apatite solubility models for the investigated MGDC rocks (Table S3).

6.2.1. Zircon Geothermometry

The relatively modest Zr concentrations in the investigated gabbro-diorite suites (average of all samples = 126 ppm) signpost their derivation from a low-temperature melt. The zircon geothermometer of Waston and Harrison [107], refined by Boehnke et al. [119], links zircon solubility in felsic to mafic rocks dominantly to melt composition and temperature, with no apparent effects due to pressure or water content, which is further confirmed by more recent experimentations/models [115–117,120–122].

Zr and Hf are mostly incompatible and typically retained in residual silicate melts until the onset of zircon saturation [107,119,120,123]. However, and in contrast to experimental data, syn-magmatic zircon crystals flourish in various primitive mafic and ultramafic rocks, even as inclusions in early-formed major minerals, thus implying zircon precipitation before the bulk mafic melt reaches zircon-saturation (e.g., [124–126]).

The calculated zircon crystallization temperatures of the analyzed gabbro-quartz diorite-diorite samples using both the original Watson and Harrison [107] model and its enhanced version of Boehnke et al. [119] are presented in Table S3. Nevertheless, we investigated, herein, the second revised model, as its starting materials included additional relatively mafic compositions beside the original mafic tonalite to rhyolite melts of Watson and Harrison. Although Boehnke et al. [119] stated that their refined model estimates largely similar temperatures for most melt compositions and temperatures as that of Watson and Harrison [107], it is clear and striking that there are noticeable numerical differences between the temperatures calculated by the two models for all samples by approximately

80–100 °C, with the higher temperatures yielded by the original model (Table S3). Temperature estimates of Boehnke et al. [119] fall within a very wide range of low to medium values for the three studied G. Shahira, W. Harqus, and W. Ba'aba'a MGDCs samples, fluctuating between minimums of 481 °C, 554 °C, and 488 °C and maximums of 649 °C, 794 °C, and 710 °C, with averages of 554 °C, 666 °C, and 580 °C, respectively. These assortments of diverse crystallization temperatures in each of the three MGCDs strongly suggest incorporation of xenocrystic zircon, either as refractory entrapped from the source or due to crustal contamination during magma extraction and storage. The noticeably moderate to low zircon saturation temperatures of these intermediate-mafic rocks, along with their low Zr abundances, may result from low-temperature crustal contamination/assimilation, which leads to the incomplete dissolution of the refractory zircon.

6.2.2. Apatite Geothermometry

The temperature at which a silicate melts, reaches saturation, and crystallizes apatite can be simply calculated for most magma compositions. Phosphorus is far more soluble in hot mafic magmas than in cooler felsic ones, and peraluminous and peralkaline melts may dissolve considerably more P than metaluminous melts [108,111,127–130].

The experimentations of Harrison and Watson [108] evidenced that for melts of basic-felsic composition (SiO2: 45–75 wt.%), 0–10 wt.% water content, and for the spectrum of pressures conceivable in the crust, the apatite solubility could be mathematically formulated as a function of temperature and the direct P2O5 and SiO2 concentrations whereupon the apatite crystallizes. However, the empirical solubility equation proposed by Harrison and Watson [108] was presumed to be applicable only in the case of metaluminous and peralkaline rocks (i.e., A/CNK < 1) [110,111,127]. Each of the three aforementioned cited studies has suggested corrections to Harrison and Watson's apatite saturation model and provided a revised equation that precisely fits for peraluminous melts (A/CNK > 1). Herein, the equation for apatite saturation in peraluminous melts provided by Pichavant et al. [111] is thought to be the optimum relative to two others since it is derived from experiments conducted at a larger array of temperatures and pressures (750–1000 °C, 2–5 kbar).

Based on their alumina saturation (A/CNK; Table S1), the studied MGDC rocks are predominantly metaluminous, with three exceptional slightly peraluminous samples from W. Harqus (A/CNK = 1.04–1.09). Accordingly, we properly calculated the apatite saturation temperatures using the Harrison and Watson [108] or Pichavant et al. [111] equations, depending on the A/CNK values of each sample. Surprisingly, as in the case of the zircon saturation geothermometer and even much more, the resultant apatite saturation temperatures span a very wide spectrum of low to high values for the G. Shahira, W. Harqus, and W. Ba'aba'a complexes. Temperature estimates for the three studied G. Shahira, W. Harqus, and W. Ba'aba'a MGDCs fluctuate between minimums of 545 °C, 742 °C, and 453 °C and maximums of 932 °C, 957 °C, and 918 °C, with averages of 725 °C, 824 °C, and 743 °C, respectively (Table S3).

Taking into consideration that most apatite crystallizes across a limited temperature interval below the saturation temperatures [128], these hotchpotches of varied temperatures, similar to zircon, indicate two genetic types of apatite in the magma: cognate and xenocrystic (sourced from the county rock). All in all, and with no exception, the calculated apatite saturation temperatures markedly exceeded zircon ones for all of the studied rock samples, implying earlier magmatic separation of apatite prior to zircon (Table S3).

6.3. Tectonic Setting

The undeniable hydrous nature of the melts from which these gabbro-diorite suites were crystallized is manifested by their marked abundance of amphiboles, mainly hornblende (up to 33.5 vol.%; Table 1), together with the discerned trace element contents and ratios characteristic of arc magmas.

Although the water content in the lithospheric and asthenospheric mantles is below 0.1 wt.% and in the continental crust < 0.001 wt.% [131], magmas must contain an apprecia-

ble amount of water (>3 wt.%) for the crystallization of hornblende [132,133]. Normally, the H_2O of arc magma is produced through the dehydration of hydrous minerals, which are brought down by the subducted oceanic slab. This water is liberated into the overlaying mantle wedge, where melting commences and hydrous magma forms [132,134]. Consequently, a subduction zone is the proper setting to generate these magmas, where further hydration for the magma can arise through metasomatism of the mantle wedge by the slab-derived fluid [132,133,135,136].

The investigated metagabbro-diorite suites show many of the geochemical aspects of the arc-type magmas. These characteristics include their strong enrichment of LILE (Cs, Rb, Ba, K, Sr) and Th and U and marked depletion in HFSE (Zr, Nb, Y, Ti) relative to N-MORB values, negative Nb and Ti anomalies, distinct positive Pb and Sr spikes, and a varied array of Zr contents (Figure 8) [137,138]. Furthermore, they exhibit rather steep LREE-enriched and HREE-depleted concentrations relative to N-MORB similar to thick-crust arcs (>39 km, i.e., continental arcs) in opposition to the flat patterns across the entire LREE-HREE range and the characteristics of thin-crust arcs (<28 km) [139].

Figure 10 illustrates plots of the investigated samples on selected widely used tectonic discrimination diagrams based on several combinations of rather immobile trace elements. In the Hf/3-Th-Ta plot [140], most of the analyzed samples (34 out of 37) cluster in the convergent plate margin fields and, more specifically, in the calc-alkaline island arcs field, rather than the primitive arc tholeiites (Figure 10a). This outcome is also observed in the Nb/Yb versus Th/Yb diagram (Figure 10b in Pearce [97]), where all samples plot far above the MORB-OIB array, which is typically found in arc-related rocks that interacted with the continental crust during ascent. Moreover, the vast majority of samples fall in the continental arcs field, although few samples are plotted outside but adjoining it, in favor of the oceanic arcs due to their high Th/Yb and Nb/Yb ratios. Even though some samples with high La/Yb values plot on the "alkaline arcs" field (c.f., [35]), none plot in the "oceanic arcs" field, and the remainder of samples plot in the "continental arcs" field, confirming the affinity of these rocks to the continental arc setting on the La/Yb-Nb/La diagram of Hollocher et al. [141] for basalts (Figure 10c). While the aforementioned tectonic setting discrimination diagrams are adapted for magmatic rocks of basaltic composition, the more evolved diorites and quartz diorites (SiO_2 > 52 wt.%) from the three studied MGDCs are correspondingly plotted in the same fields as the gabbros. Using the Ta + Yb vs. Rb diagram for tectonic discrimination for granitic rocks of Pearce et al. [142], all samples, including those with SiO_2 contents higher than 52 wt.%, plot in the volcanic arc field (Figure 10d), confirming the continental arc setting inferred from the previously employed tectonic discrimination diagrams of basalts.

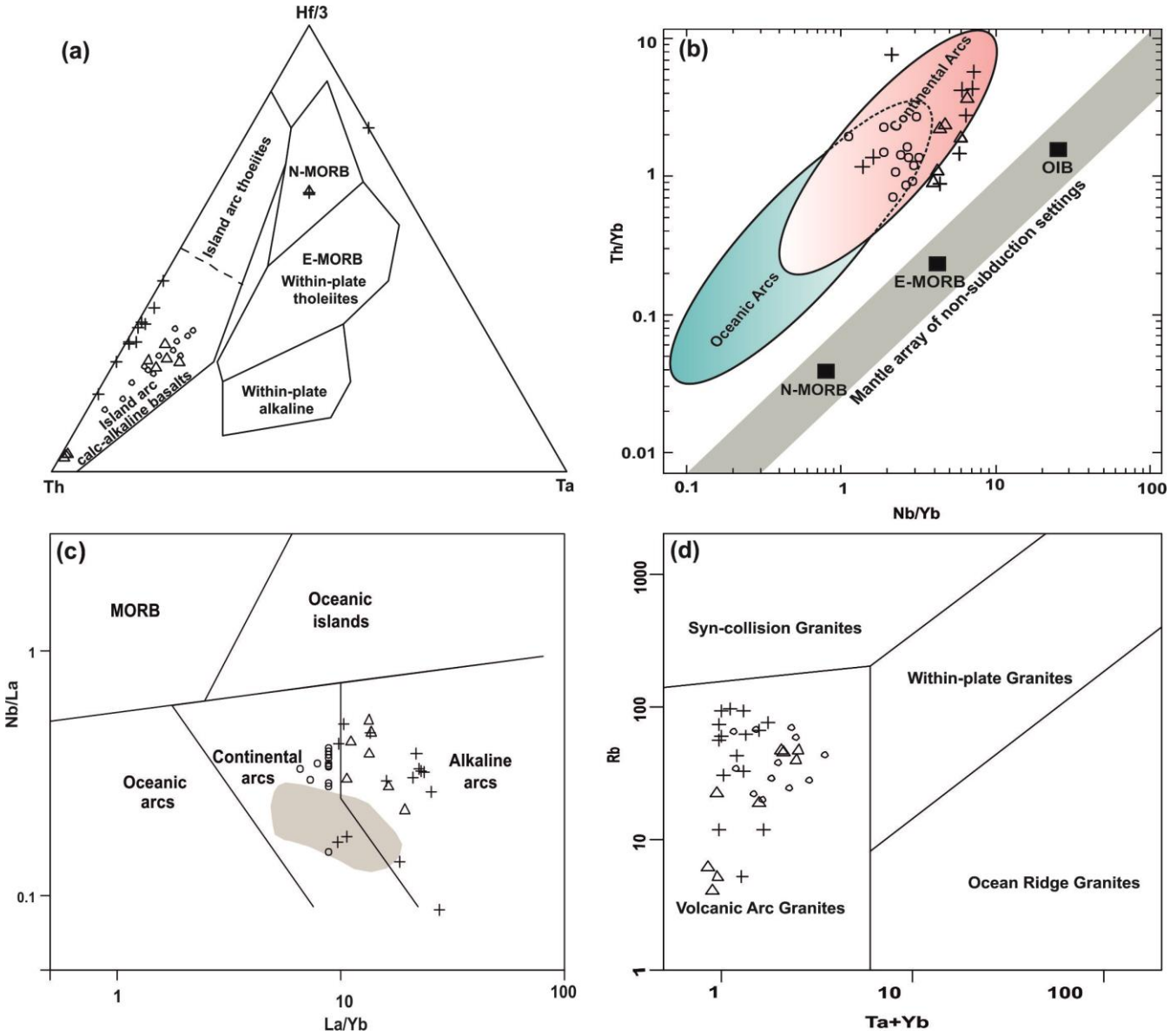


Figure 10. Tectonic discrimination diagrams of the three investigated gabbro-diorite complexes in Sinai: (**a**) Hf/3-Th/Ta/16 diagram [140], (**b**) Nb/Yb versus Th/Yb diagram of Pearce [97], (**c**) La/Yb versus Nb/La diagram of Hollocher et al. [141], (**d**) Ta + Yb-Rb diagram of Pearce et al. [142]. The gray field in (**c**) represents the Um Balad gabbro-diorite complex from the north Eastern Desert (12 samples) after Abd El-Rahman et al. [35]. Symbols as in Figure 4.

6.4. Parental Magma and Source Characteristics

Arc magmas generated at active continental margins, such as the investigated MGDCs, may comprise components derived from melting of the mantle wedge (both sub-continental lithospheric and asthenospheric mantle), subducting oceanic lithosphere, subducted overlying sediments, and continental crust (e.g., [138,143–148]). The subducted oceanic slab and sediments (i.e., subduction component) comprise substantial amounts of volatiles (e.g., H_2O, CO_2) and LILEs (e.g., Cs, Ba, Rb, and Sr) [138,149], whereas the continental crust component is delivered during the ascent of parent mantle melts in the crust.

6.4.1. Mantle Source

The studied metagabbro-diorite complexes have HREE concentrations lower than N-MORB (Figure 9), which implies derivation from a sub-arc mantle, which is more HREE-

depleted relative to the MORB-type mantle. Depletion in a convicting mantle wedge is prevalent beneath both continental and oceanic arcs [150,151]. Participation of garnet during the evolution of arc magmas is another likelihood to explain the depletion in HREE [152,153].

The Rb/Sr ratios of the studied MGDC samples fall within a limited range of very low values (0.01–0.13), with an average of 0.06 (Table S2). Considering that mantle materials retain exceptionally low Rb/Sr ratios (0.1–0.01; [154,155]), and the depleted mantle further possesses an extremely lower value (0.01; [156]), while the lower and middle continental crusts have higher Rb/Sr ratios of 0.12 and 0.22, respectively [72,157], such Rb/Sr ratios imply major input of mantle material in the genesis of these gabbro-diorite suites. Also, the Ba/Rb ratios of the studied gabbro-diorite suites (4.6–28.5) average 13.5, which is closely comparable to the mantle value (Ba/Rb = 11; [158]), but is considerably higher than the average crustal estimate (Ba/Rb = 6.7; [72]). The mantle and mantle-derived melts have typically high chondritic to superchondritic Nb/Ta ratios (>17.5) [155,159], whereas the typical Nb/Ta ratio of the continental crust seems to be appreciably below the chondritic value (11–12; [64,72,82,154,159]). The Nb/Ta ratios of the studied gabbro-diorite suites fluctuate widely between 18.73 and 10.81 (average = 14.3), which may suggest derivation from a mantle source that was later modified by crustal contamination.

The Nb/La ratio has been demonstrated to be efficient in discriminating between magmas derived from lithospheric mantles (low Nb/La: <0.4) and asthenospheric mantles (high Nb/La: >1) [160]. Herein, all of the analyzed MGDC samples exhibit low Nb/La ratios (0.15–0.52; average = 0.28), implying a lithospheric mantle source. The heavy REE is obviously depleted relative to the middle REE (Figure 9), indicating the presence of garnet in the source and its dissolution during partial melting since HREE is highly compatible with garnet. This may suggest that for a mantle source, a somewhat deep mantle is more likely than a shallow one where garnet stability is favored instead of spinel [153,161,162]. Furthermore, it has been revealed that partial melting of mantle lherzolite in the garnet stability field will produce melts with a high Dy/Yb ratio (>2.5), whereas mantle lherzolite that undergoes melting in the spinel stability field will generate melts with lower Dy/Yb values (<1.5) [163–165]. Table S2 reveals that the Dy/Yb ratios of the analyzed MGDC samples fall within the range 1.19–3.01 with an average value of 2.2, with many samples having Dy/Yb ratios > 2.5 (n = 9). This implies that the parental magmas of these gabbro-diorites originated from the remelting of a spinel–garnet transitional mantle source at a depth of ca. 75–90 km (c.f., [166,167].

6.4.2. Subduction Component

The depleted mantle wedge can be affected by descending oceanic slabs through (1) the fluxing of fluids and/or hydrous melts [168–170] and (2) the addition of pelagic sediments [144,171–174]. This subduction component leads to the substantial addition of volatiles and LILEs to the evolved arc magma.

Fundamentally, the prevalent calc-alkaline affinity, Pb enrichment, and negative Nb-anomalies in the analyzed samples verify sources influenced by subduction processes and crustal contamination. Th/Yb is a criterion for subduction component, while Nb/Yb is a proxy for mantle contribution; hence, the Th/Yb versus Nb/Yb plot can be used to assess the incorporation of subduction-derived materials and continental crust contamination [97,175]. The evident enrichment in Th led to the plot of the studied gabbro-diorite rocks above the MORB-OIB array within the field of continental arcs in the Th/Yb-Ta/Yb diagram (Figure 10b), which is related to an appreciable contribution of the subducting slab to the mantle wedge.

LILE are more readily mobilized from the slab and transported to the mantle wedge if the metasomatizing agents are hydrous fluids, unlike HFSE, which are immobile because of their little compatibility with hydrous fluids. The marked enrichment in the LILE (Figure 8) and high Sr/Nd ratios (average = 33.6) suggest that the parent magma of these metagabbro-diorite complexes was evolved from the sub-arc mantle wedge metasomatized

by dehydration of subducted basaltic ocean crust rather than by subducted terrigenous sediment (e.g., [176–178]). Moreover, certain trace element ratios are proved to be sensitive to mantle wedge metasomatism either by hydrous fluids (fluid-induced metasomatism) (e.g., Rb/Yb, Ba/La, La/Yb), or slab melting (melt-induced metasomatism (e.g., Nb/Y, Th/Yb, La/Yb), and are universally used to track subducted/subducting slab melts and fluids [179–182]. Figure 11 shows plots of the studied samples on three diagrams based on these diagnostic trace element ratios (Nb/Y vs. Rb/Y, Ba/La vs. Th/Yb, and La/Yb vs. Nb/Y). In all these plots, it is evident that the impact of slab-derived fluids is much greater than that of slab-derived melts. Consequently, subduction-related fluids implemented a crucial effect on metasomatizing the partially melted mantle source, sustaining the investigated metagabbro-diorite complexes with their subduction-related signatures.

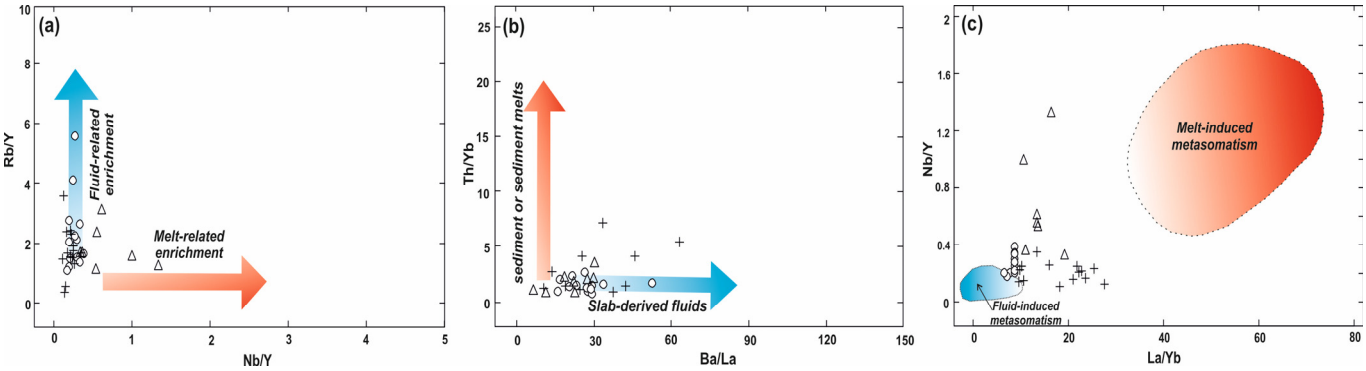


Figure 11. Revealing the effect of slab components on mantle wedge metasomatism through plotting the analyzed samples on some diagnostic trace elemental ratio diagrams: (**a**) Nb/Y vs. Rb/Y [180], (**b**) Ba/La vs. Th/Yb [179], and (**c**) La/Yb vs. Nb/La [181]. Symbols as in Figure 4.

6.5. Role of Crustal Contamination

The ultimate source of compositional modification in the investigated MGDCs magma is crustal contamination. This is because mantle-metasomatized melts in continental arc settings, such as the studied MGDCs, can hardly abstain from interaction with the crust in the course of their ascent through or storage in the thick and lithologically varied continental lithosphere.

The relative enrichment in Th shown by clustering of the studied samples close to the Th-apex in the Th-Hf-Ta diagram of Wood [140] (Figure 10a) may indicate bulk contamination of mantle-derived basic magmas by the relatively Th-rich upper crust [183]. The Th/Ta ratio is a significant indicator of mantle–crust interaction, as mantle-derived rocks are likely to retain uniformly low Th/Ta ratios approaching 2, whereas lower and upper continental crusts have higher values (Th/Ta = 7.9 and 6.9, respectively) [184]. Most of the studied samples exhibit high to very high Th/Ta ratios (up to 36.7), with an average value of 6.15 (Table S2), which implies significant crustal contamination.

In closed magmatic systems, the ratio of strongly to fairly incompatible elements will remain more or less constant or slightly change. Accordingly, ratios like Ba/Nb, Rb/Y, and Rb/Zr will not substantially vary by simple fractional crystallization, while fluctuations in these ratios are expectedly related to crustal contamination via assimilation-fractional crystallization processes [185]. Figure 12a,b) reveals that the investigated metagabbro-diorite rocks, although few samples display scattering, exhibit general positive variations in the Ba/Nb and Rb/Zr ratios with increasing silica, which denote a role of crustal contamination during their magmatic evolution (Figure 13).

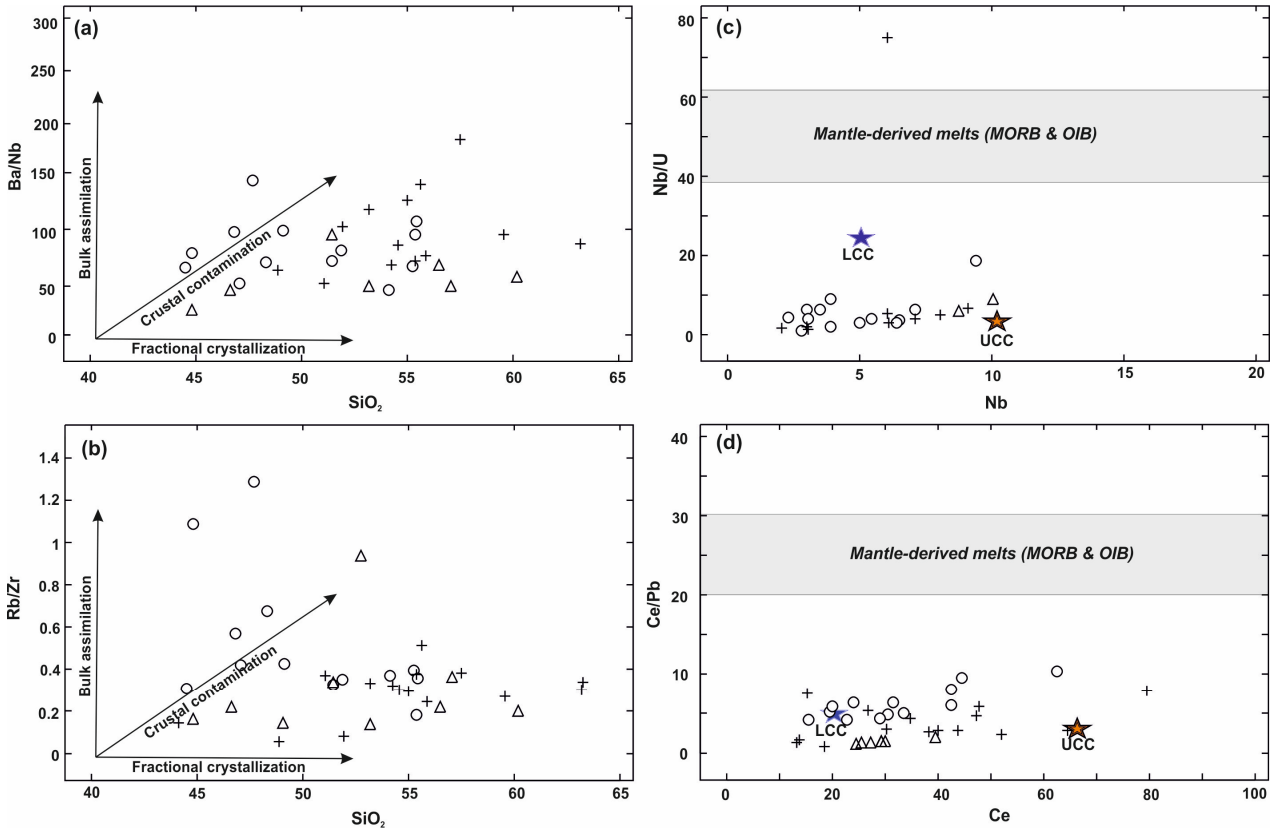


Figure 12. (**a**,**b**): SiO_2 vs. Ba/Nb and Rb/Zr variation diagrams for the studied MGDC samples. Solid line vectors show the expected trends for fractional crystallization and crustal contamination/assimilation. (**c**,**d**): Nb/U vs. Nb and Ce/Pb vs. Ce diagrams for the studied samples. Data for the upper and lower continental crusts (UCC and LCC, respectively) are from Rudnick and Gao [64], and data for MORB and OIB are from Hofmann et al. [186].

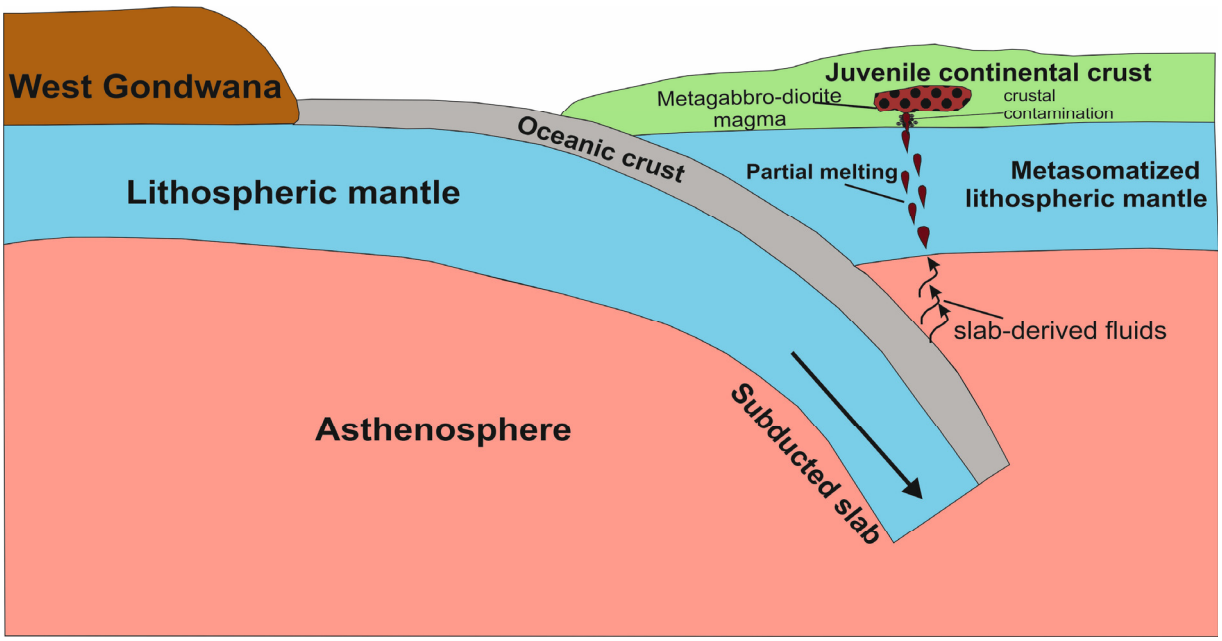


Figure 13. Simplified sketch model illustrating the tectono-magmatic evolution of the metagabbro-diorite complexes in continental arc setting during the late Neoproterozoic (southern Sinai, NE Arabian-Nubian Shield). See text for further explanation.

The Ce/Pb and Nb/U ratios are deemed the finest and appropriate trace element markers to promptly assess the impact of crustal assimilation on mantle-derived rocks, as they possess constrained ranges of high values of these ratios (Ce/Pb: 25 ± 5 and Nb/U: 47 ± 10; [186]) while continental crust has substantially lower Ce/Pb and Nb/U ratios (3.9 and 6.2, respectively; [64]). Apart from one bizarre sample having extraordinary Nb/U value (>70), all the studied samples possess relatively low Nb/U and Ce/Pb ratios approaching those of upper and lower continental crust (Table S2; Figure 12c,d), indicating subjection of their mantle-derived magma to substantial crustal contamination as a dominant mechanism of differentiation (c.f., [55,187–189]) (Figure 13).

7. Conclusions

The following points summarize the main conclusions reached in this contribution:

1—The three complexes vary in the dominance of the gabbroic versus dioritic rock types among each one. For instance, in the W. Ba'aba'a and Wadi Harqus complexes, they are represented by melanocratic diorites that pass into more basic gabbro with gradational diffused contacts. In the Shahira complex, gabbros strongly predominate over diorites and display both isotropic and layered varieties.

2—Petrographically, gabbroids are distinguished into pyroxene-hornblende gabbros and hornblende gabbros based on the relative proportions of hornblende and pyroxene, whereas dioritic rocks have been subdivided on the basis of modal quartz contents into diorites and quartz diorites.

3—The studied MGDC rock samples possess a prevalent calc-alkaline character over subsidiary tholeiitic ones, although some samples (n = 7) from W. G. Shahira and W. Hurqus show mild alkaline affinity. Regarding alumina saturation, apart from three peraluminous samples (A/CNK > 1) from W. Harqus, the studied MGDC rocks are metaluminous with A/CNK < 1 and A/NK > 1 and usually have normative titanite ± diopside and lack normative corundum.

4—Among the studied MGDCs, G. Shahira MGDC samples exhibit higher abundances and averages of the compatible transition metals Ni (average = 57.14 ppm), Cr (average = 115.63 ppm), Sc (average = 26.74 ppm), and V (average = 247.97 ppm) compared with those of W. Ba'aba'a and W. Harqus, and conversely possess lower abundances and averages of the high field strength elements (HFSE) Zr (average = 85.79 ppm) and Nb (average = 4.79 ppm). In addition, the most distinctive and mutual features in the profiles of the investigated MGDCs on the N-MORB-normalized incompatible multi-element spider diagrams are the distinctly deep negative Nb anomalies and the projecting positive Pb spikes.

5—Although the samples from the three MGDCs exhibit variably LREE-enriched patterns [$(La/Yb)_N$ = 4.92–18.55; av. = 9.04], the samples of G. Shahira show almost parallel smooth patterns, in opposition to the subparallel kinked patterns with alternative Gd-Tb and Er-Tm plateaus and a Dy-Ho trough in between for the W. Ba'aba'a and W. Harqus samples. Likewise, G. Shahira REE patterns lack Eu anomalies ($Eu/Eu^* \approx 1$), while the other two MGDCs show weak to negligible positive and negative Eu anomalies.

6—Various geochemical criteria, including their low loss on ignition (LOI) values, lack of Ce anomalies, low values of the LREE/HREE ratio, and near-chondritic Y/Ho and Zr/Hf ratios, suggest that post-magmatic alteration did not have a significant impact on the investigated samples.

7—The calculated apatite and zircon crystallization temperatures reveal the earlier separation of apatite at higher temperatures for the three studied complexes. However, both accessories have yielded very wide ranges of crystallization temperatures, which may indicate two genetic types of apatite and zircon in the magma: cognate and xenocrystic.

8—The investigated metagabbro-diorite complexes were formed in a continental arc setting, particularly a thick-crust arc (>39 km).

9—The parent magmas comprised components derived from the melting of the mantle wedge, subducting oceanic lithosphere, and subducting overlying sediments. The mantle input was from a spinel–garnet transitional mantle source at a depth of ca. 75–90 km.

10—The impact of slab-derived fluids was much greater than that of slab-derived melts. Consequently, subduction-related fluids had a crucial effect on metasomatizing the partially melted mantle source.

11—During ascent and storage in the crust, the parent mantle-derived magma has been subjected to substantial crustal contamination as a dominant mechanism of differentiation.

Supplementary Materials: The following supporting information can be downloaded at: https://www.mdpi.com/article/10.3390/min14020145/s1. Table S1: Major element composition (wt.%), calculated CIPW normative minerals, calculated apatite crystallization temperatures, and significant elemental ratios and indices of the studied metagabbro-diorite complex rocks; Table S2: Trace and REE element contents (ppm), calculated zircon crystallization temperatures, and some elemental ratios of the studied metagabbro-diorite complex rocks; Table S3: Calculated zircon and apatite crystallization temperature of the studied metagabbro-diorite complex rocks.

Author Contributions: Conceptualization, M.Z.E.-B.; Writing—review and editing, M.Z.E.-B., M.Z.K., H.F.H. and B.M.E.-B. Field work and sample collection, M.Z.E.-B. and H.F.H. Microscopic investigations, M.Z.E.-B. Sample preparation for chemical analysis, M.Z.E.-B.; data processing and diagram plotting, M.Z.E.-B. and B.M.E.-B. All authors have read and agreed to the published version of the manuscript.

Funding: This research received no external funding.

Data Availability Statement: All data derived from this research are presented in the enclosed figures and tables, as well as in Supplementary Materials.

Acknowledgments: Mohammed El-Bialy likes to express his thanks to Sherif M. Abdou for his help and assistance during the fieldwork in the Wadi Ba'ab'a area and to Hajj Abdul-Rahman Issa, who was a highly professional and honest off-road driver. Thanks should go to two anonymous reviewers, whose comments and careful reviews helped improve the manuscript.

Conflicts of Interest: The authors declare no conflict of interest.

References

1. Stern, R.J. Arc assembly and continental collision in the Neoproterozoic east African orogen: Implications for the Consolidation of Gondwanaland. *Annu. Rev. Earth Planet. Sci.* **1994**, *22*, 319–351. [CrossRef]
2. Stern, R.J. Crustal Evolution in the East African Orogen: A Neodymium Isotopic Perspective. *J. Afr. Earth Sci.* **2002**, *34*, 109–117. [CrossRef]
3. Hargrove, U.S.; Stern, R.J.; Kimura, J.-I.; Manton, W.I.; Johnson, P.R. How Juvenile Is the Arabian–Nubian Shield? Evidence from Nd Isotopes and Pre-Neoproterozoic Inherited Zircon in the Bi'r Umq Suture Zone, Saudi Arabia. *Earth Planet. Sci. Lett.* **2006**, *252*, 308–326. [CrossRef]
4. Be'eri-Shlevin, Y.; Katzir, Y.; Valley, J.W. Crustal Evolution and Recycling in a Juvenile Continent: Oxygen Isotope Ratio of Zircon in the Northern Arabian Nubian Shield. *Lithos* **2009**, *107*, 169–184. [CrossRef]
5. Be'eri-Shlevin, Y.; Eyal, M.; Eyal, Y.; Whitehouse, M.J.; Litvinovsky, B. The Sa'al Volcano-Sedimentary Complex (Sinai, Egypt): A Latest Mesoproterozoic Volcanic Arc in the Northern Arabian Nubian Shield. *Geology* **2012**, *40*, 403–406. [CrossRef]
6. Johnson, P.R.; Andresen, A.; Collins, A.S.; Fowler, A.R.; Fritz, H.; Ghebreab, W.; Kusky, T.; Stern, R.J. Late Cryogenian–Ediacaran History of the Arabian–Nubian Shield: A Review of Depositional, Plutonic, Structural, and Tectonic Events in the Closing Stages of the Northern East African Orogen. *J. Afr. Earth Sci.* **2011**, *61*, 167–232. [CrossRef]
7. Abdelsalam, M.G.; Stern, R.J. Sutures and Shear Zones in the Arabian-Nubian Shield. *J. Afr. Earth Sci.* **1996**, *23*, 289–310. [CrossRef]
8. Peng, P.; Anbar, M.M.A.; He, X.-F.; Liu, X.; Qin, Z. Cryogenian Accretion of the Northern Arabian-Nubian Shield: Integrated Evidence from Central Eastern Desert Egypt. *Precambrian Res.* **2022**, *371*, 106599. [CrossRef]
9. Stoeser, D.B.; Frost, C.D. Nd, Pb, Sr, and O Isotopic Characterization of Saudi Arabian Shield Terranes. *Chem. Geol.* **2006**, *226*, 163–188. [CrossRef]
10. Avigad, D.; Gvirtzman, Z. Late Neoproterozoic Rise and Fall of the Northern Arabian–Nubian Shield: The Role of Lithospheric Mantle Delamination and Subsequent Thermal Subsidence. *Tectonophysics* **2009**, *477*, 217–228. [CrossRef]
11. Avigad, D.; Sandler, A.; Kolodner, K.; Stern, R.; Mcwilliams, M.; Miller, N.; Beyth, M. Mass-Production of Cambro–Ordovician Quartz-Rich Sandstone as a Consequence of Chemical Weathering of Pan-African Terranes: Environmental Implications. *Earth Planet. Sci. Lett.* **2005**, *240*, 818–826. [CrossRef]
12. El-Bialy, M.Z. On the Pan-African Transition of the Arabian–Nubian Shield from Compression to Extension: The Post-Collision Dokhan Volcanic Suite of Kid-Malhak Region, Sinai, Egypt. *Gondwana Res.* **2010**, *17*, 26–43. [CrossRef]

13. Eyal, M.; Litvinovsky, B.; Jahn, B.M.; Zanvilevich, A.; Katzir, Y. Origin and Evolution of Post-Collisional Magmatism: Coeval Neoproterozoic Calc-Alkaline and Alkaline Suites of the Sinai Peninsula. *Chem. Geol.* **2010**, *269*, 153–179. [CrossRef]
14. Eliwa, H.A.; El-Bialy, M.Z.; Murata, M. Edicaran Post-Collisional Volcanism in the Arabian-Nubian Shield: The High-K Calc-Alkaline Dokhan Volcanics of Gabal Samr El-Qaa (592 ± 5Ma), North Eastern Desert, Egypt. *Precambrian Res.* **2014**, *246*, 180–207. [CrossRef]
15. Zoheir, B.; Zeh, A.; El-Bialy, M.; Ragab, A.; Deshesh, F.; Steele-MacInnis, M. Hybrid Granite Magmatism during Orogenic Collapse in the Eastern Desert of Egypt: Inferences from Whole-Rock Geochemistry and Zircon U–Pb–Hf Isotopes. *Precambrian Res.* **2021**, *354*, 106044. [CrossRef]
16. Basta, E.Z.; Takla, M.A. Distribution of Opaque Minerals and the Origin of the Gabbroic Rocks of Egypt. *Bull. Fac. Pharm. Cairo Univ.* **1974**, *47*, 347–364.
17. Takla, M.A.; Basta, E.; Fawzi, E. Characterization of the Older and Younger Gabbros of Egypt. *Delta J. Sci.* **1981**, *5*, 279–314.
18. Khalil, A.E.S.; Obeid, M.A.; Azer, M.K. Late Neoproterozoic Post-Collisional Mafic Magmatism in the Arabian–Nubian Shield: A Case Study from Wadi El-Mahash Gabbroic Intrusion in Southeast Sinai, Egypt. *J. Afr. Earth Sci.* **2015**, *105*, 29–46. [CrossRef]
19. Samuel, M.D.; Sadek Ghabrial, D.; Moussa, H.E.; Ali-Bik, M.W. The Petrogenesis of Late Neoproterozoic Gabbro/Diorite Intrusion at Sheikh El-Arab Area, Central Sinai, Egypt. *Arab. J. Geosci.* **2015**, *8*, 5579–5599. [CrossRef]
20. Azer, M.K.; Surour, A.A.; Madani, A.A.; Ren, M.; El-Fatah, A.A.A. Mineralogical and Geochemical Constraints on the Postcollisional Mafic Magmatism in the Arabian-Nubian Shield: An Example from the El-Bakriya Area, Central Eastern Desert, Egypt. *J. Geol.* **2022**, *130*, 209–230. [CrossRef]
21. Surour, A.A.; Ahmed, A.H.; Harbi, H.M. Mineral Chemistry as a Tool for Understanding the Petrogenesis of Cryogenian (Arc-Related)–Ediacaran (Post-Collisional) Gabbros in the Western Arabian Shield of Saudi Arabia. *Int. J. Earth Sci.* **2017**, *106*, 1597–1617. [CrossRef]
22. Gahlan, H.A.; Obeid, M.A.; Azer, M.K.; Asimow, P.D. An Example of Post-Collisional Appinitic Magmatism with an Arc-like Signature: The Wadi Nasb Mafic Intrusion, North Arabian–Nubian Shield, South Sinai, Egypt. *Int. Geol. Rev.* **2018**, *60*, 865–888. [CrossRef]
23. Ragab, A. The Role of Post-Collisional Mafic Magmatism in the Late Stages of Evolution of the Northernmost Arabian-Nubian Shield (ANS): A Case Study from Isla Complex, Wadi Isla, South Sinai, Egypt. *J. Afr. Earth Sci.* **2020**, *164*, 103768. [CrossRef]
24. Abdelfadil, K.M.; Saleh, G.M.; Putiš, M.; Sami, M. Mantle Source Characteristics of the Late Neoproterozoic Post-Collisional Gabbroic Intrusion of Wadi Abu Hadieda, North Arabian-Nubian Shield, Egypt. *J. Afr. Earth Sci.* **2022**, *194*, 104607. [CrossRef]
25. Ali, S.; Abart, R.; Sayyed, M.I.; Hauzenberger, C.A.; Sami, M. Petrogenesis of the Wadi El-Faliq Gabbroic Intrusion in the Central Eastern Desert of Egypt: Implications for Neoproterozoic Post-Collisional Magmatism Associated with the Najd Fault System. *Minerals* **2022**, *13*, 10. [CrossRef]
26. El Gaby, S.; Tehrani, R.; List, F.K. The Basement Complex of the Eastern Desert and Sinai. In *The Geology of Egypt*; Balkema: Rotterdam, The Netherlands, 1990; pp. 175–184.
27. Furnes, H.; El-Sayed, M.M.; Khalil, S.O.; Hassanen, M.A. Pan-African Magmatism in the Wadi El-Imra District, Central Eastern Desert, Egypt: Geochemistry and Tectonic Environment. *J. Geol. Soc.* **1996**, *153*, 705–718. [CrossRef]
28. El Sharkawy, M.A.; El Bayoumi, R.M. The Ophiolites of Wadi Ghadir Area, Eastern Desert, Egypt. *Ann. Geol. Surv. Egypt* **1979**, *9*, 125–135.
29. Zoheir, B.A.; Mehanna, A.M.; Qaoud, N.N. Geochemistry and Geothermobarometry of the Um Eleiga Neoproterozoic Island Arc Intrusive Complex, SE Egypt: Genesis of a Potential Gold-Hosting Intrusion. *Appl. Earth Sci.* **2008**, *117*, 89–111. [CrossRef]
30. Kharbish, S. Geochemistry and Magmatic Setting of Wadi El-Markh Island-Arc Gabbro–Diorite Suite, Central Eastern Desert, Egypt. *Chem. Der Erde—Geochem.* **2010**, *70*, 257–266. [CrossRef]
31. Obeid, M. Petrogenesis of Bir Madi Gabbro-Diorite and Tonalite-Granodiorite Intrusions in Southeastern Desert, Egypt&58; Implications for Tectono-Magmatic Processes at the Neoproterozoic Shield. *Int. J. Econ. Environ. Geol.* **2010**, *1*, 27–35.
32. Basta, F.; Maurice, A.; Bakhit, B.; Azer, M.; El-Sobky, A. Intrusive Rocks of the Wadi Hamad Area, North Eastern Desert, Egypt: Change of Magma Composition with Maturity of Neoproterozoic Continental Island Arc and the Role of Collisional Plutonism in the Differentiation of Arc Crust. *Lithos* **2017**, *288–289*, 248–263. [CrossRef]
33. Stern, R.J.; Ali, K.; Asimow, P.D.; Azer, M.K.; Leybourne, M.I.; Mubarak, H.S.; Ren, M.; Romer, R.L.; Whitehouse, M.J. The Atud Gabbro–Diorite Complex: Glimpse of the Cryogenian Mixing, Assimilation, Storage and Homogenization Zone beneath the Eastern Desert of Egypt. *J. Geol. Soc.* **2020**, *177*, 965–980. [CrossRef]
34. Abdel-Karim, A.-A.; Azer, M.; Megahed, M.; Mogahed, M. Neoproterozoic Concentric Intrusive Complex of Gabbro-Diorite-Tonalite-Granodiorite Association, Rahaba Area, Southern Eastern Desert of Egypt: Implications for Magma Mixing of Arc Intrusive Rocks. *Lithos* **2021**, *404–405*, 106423. [CrossRef]
35. Abd El-Rahman, Y.; Seifert, T.; Schulz, B.; Zieger-Hofmann, M.; Gärtner, A.; Linnemann, U.; Said, A. Petrogenesis of the Late Tonian Arc-Related Um Balad Gabbro-Diorite Complex (Egypt) and Insight into Its Spatially Related Orogenic Gold Mineralization. *Int. Geol. Rev.* **2023**, *65*, 89–113. [CrossRef]
36. Azer, M.; Obeid, M.; Gahlan, H. Late Neoproterozoic Layered Mafic Intrusion of Arc-Affinity in the Arabian-Nubian Shield: A Case Study from the Shahira Layered Mafic Intrusion, Southern Sinai, Egypt. *Geol. Acta* **2016**, *14*, 237–259. [CrossRef]
37. Lebda, E.-M.; Ghoneim, M.; Abdel-Karim, A.-A. Gabbros versus Granites of the Subduction Regime of South Sinai, Egypt: Discrimination and Geochemical Modelling. *Arab. J. Geosci.* **2019**, *12*, 551. [CrossRef]

38. Ghoneim, M.; Anbar, M.M.; Hamdy, D.; Masoud, A. Petrogenesis and Tectonic Implications of Seih Syn-Tectonic Gabbroic Intrusion, South Sinai, Egypt: Insights from Whole-Rock Geochemistry, Mineral Chemistry, and P-T Estimate. *Delta J. Sci.* **2021**, *43*, 1012–5965. [CrossRef]
39. Abu-Ela, F. Neoproterozoic Tholeiitic Arc Plutonism: Petrology of Gabbroic Intrusions in the El-Aradiya Area, Eastern Desert, Egypt. *J. Afr. Earth Sci.* **1999**, *28*, 721–741. [CrossRef]
40. Abdel-Rahman, A.-F. Petrogenesis of Early-Orogenic Diorites, Tonalites and Post-Orogenic Trondhjemites in the Nubian Shield. *J. Petrol.* **1990**, *31*, 1285–1312. [CrossRef]
41. Abu El-Ela, F.F. Geochemistry of an Island-Arc Plutonic Suite: Wadi Dabr Intrusive Complex, Eastern Desert, Egypt. *J. Afr. Earth Sci.* **1997**, *24*, 473–496. [CrossRef]
42. Abdelnasser, A.; Kumral, M. Mineral Chemistry and Geochemical Behavior of Hydrothermal Alterations Associated with Mafic Intrusive-Related Au Deposits at the Atud Area, Central Eastern Desert, Egypt. *Ore Geol. Rev.* **2016**, *77*, 1–24. [CrossRef]
43. Abdel-Karim, A.-A. Late Precambrian Metagabbro-Diorite Complex from Southwest Sinai, Egypt. Egypt. *Egypt J. Geol.* **1995**, *39*, 715–738.
44. El-Bialy, M.Z. Petrologic, Geochemical and Petrogenetic Characterization of the Old Granites of Sinai, Egypt. Ph.D. Thesis, Suez Canal University, Ismailia, Egypt, 2004; 230p.
45. Shimron, A. Evolution of the Kid Group, Southeast Sinai Peninsula: Thrusts, Melanges, and Implications for Accretionary Tectonics during the Late Proterozoic of the Arabian-Nubian Shield. *Geology* **1984**, *12*, 242–247. [CrossRef]
46. Furnes, H.; Shimron, A.E.; Roberts, D. Geochemistry of Pan-African Volcanic Arc Sequences in Southeastern Sinai Peninsula and Plate Tectonic Implications. *Precambrian Res.* **1985**, *29*, 359–382. [CrossRef]
47. Khalifa, I.H.; El-Bialy, M.Z.; Hassan, D.M. Petrologic and Geochemical Characterization and Mineralization of the Metavolcanic Rocks of the Heib Formation, Kid Metamorphic Complex, Sinai, Egypt. *Geosci. Front.* **2011**, *2*, 385–402. [CrossRef]
48. El-Bialy, M.Z. Geochemistry of the Neoproterozoic Metasediments of Malhaq and Um Zariq Formations, Kid Metamorphic Complex, Sinai, Egypt: Implications for Source-Area Weathering, Provenance, Recycling, and Depositional Tectonic Setting. *Lithos* **2013**, *175–176*, 68–85. [CrossRef]
49. El-Bialy, M.Z.; Ali, K.A.; Abu El-Enen, M.M.; Ahmed, A.H. Provenance and Metamorphic PT Conditions of Cryogenian–Ediacaran Metasediments from the Kid Metamorphic Complex, Sinai, NE Arabian–Nubian Shield: Insights from Detrital Zircon Geochemistry and Mineral Chemistry. *Tectonophysics* **2015**, *665*, 199–217. [CrossRef]
50. Eliwa, H.; Abu El-Enen, M.; Khalaf, I.M.; Itaya, T. Metamorphic Evolution of Sinai Metapelites and Gneisses: Constraints from Petrology and K/Ar Dating. *Egypt. J. Geol.* **2004**, *48*, 169–185.
51. Moghazi, A.-K.M.; Ali, K.A.; Wilde, S.A.; Zhou, Q.; Andersen, T.; Andresen, A.; Abu El-Enen, M.M.; Stern, R.J. Geochemistry, Geochronology, and Sr–Nd Isotopes of the Late Neoproterozoic Wadi Kid Volcano-Sedimentary Rocks, Southern Sinai, Egypt: Implications for Tectonic Setting and Crustal Evolution. *Lithos* **2012**, *154*, 147–165. [CrossRef]
52. Bentor, Y.K.; Eyal, M. *The Geology of Southern Sinai, Its Implication for the Evolution of the Arabo-Nubian Massive. V. 1 (Jebel Sabbagh Sheet)*; The Israel Academy of Science and Humanities: Jerusalem, Israel, 1989.
53. Moghazi, A.M.; Andersen, T.; Oweiss, G.A.; El Bouseily, A.M. Geochemical and Sr–Nd–Pb Isotopic Data Bearing on the Origin of Pan-Africangranitoids in the Kid Area, Southeast Sinai, Egypt. *J. Geol. Soc.* **1998**, *155*, 697–710. [CrossRef]
54. Brooijmans, P.; Blasband, B.; White, S.H.; Visser, W.J.; Dirks, P. Geothermobarometric Evidence for a Metamorphic Core Complex in Sinai, Egypt. *Precambrian Res.* **2003**, *123*, 249–268. [CrossRef]
55. El-Bialy, M.Z.; Khalifa, I.H.; Omar, M.M. Continental Intraplate Volcanism in the Sinai Subplate: The Oligo-Miocene Basalts of the Gulf of Suez Rift. *J. Afr. Earth Sci.* **2018**, *146*, 158–179. [CrossRef]
56. Johnson, D.M.; Hooper, P.R.; Conrey, R.M. XRF Analysis of Rocks and Minerals for Major and Trace Elements on a Single Low Dilution Li-Tetraborate Fused Bead. *Adv. X-ray Anal.* **1999**, *41*, 843–867.
57. Knaack, C.; Cornelius, S.; Hooper, P. Trace Element Analyses of Rocks and Minerals by ICP-MS 1994.
58. Le Maitre, R.W.; Streckeisen, A.; Zanettin, B.; Le Bas, M.J.; Bonin, B.; Bateman, P. (Eds.) *Igneous Rocks: A Classification and Glossary of Terms*; Cambridge University Press: Cambridge, UK, 2005; 252p, ISBN 0521619483.
59. Middlemost, E.A.K. Naming Materials in the Magma/Igneous Rock System. *Earth-Sci. Rev.* **1994**, *37*, 215–224. [CrossRef]
60. Enrique, P. Una Clasificación Normativa de Las Rocas Plutónicas y Volcánicas Mediante El Diagrama 2Q-(Or+ab)-4an-2F. *Geogaceta* **2018**, *64*, 115–118.
61. Miyashiro, A. Nature of Alkalic Volcanic Rock Series. *Contrib. Miner. Petrol.* **1978**, *66*, 91–104. [CrossRef]
62. Irvine, T.N.; Baragar, W.R.A. A Guide to the Chemical Classification of the Common Volcanic Rocks. *Can. J. Earth Sci.* **1971**, *8*, 523–548. [CrossRef]
63. Thornton, C.P.; Tuttle, O.F. Chemistry of Igneous Rocks–[Part] 1, Differentiation Index. *Am. J. Sci.* **1960**, *258*, 664–684. [CrossRef]
64. Chappell, B.W. Compositional Variation within Granite Suites of the Lachlan Fold Belt: Its Causes and Implications for the Physical State of Granite Magma. *Earth Environ. Sci. Trans. R Soc. Edinb.* **1996**, *87*, 159–170. [CrossRef]
65. Wall, V.J.; Clemens, J.D.; Clarke, D.B. Models for Granitoid Evolution and Source Compositions. *J. Geol.* **1987**, *95*, 731–749. [CrossRef]
66. Rudnick, R.L.; Gao, S. Composition of the Continental Crust. *Treatise Geochem.* **2003**, *3*, 659. [CrossRef]
67. Taylor, S.R. The Application of Trace Element Data to Problems in Petrology. *Phys. Chem. Earth* **1965**, *6*, 133–213. [CrossRef]

68. Shaw, D.M. A Review of K-Rb Fractionation Trends by Covariance Analysis. *Geochim. Et Cosmochim. Acta* **1968**, *32*, 573–601. [CrossRef]
69. Clarke, D.B. The Mineralogy of Peraluminous Granites; a Review. *Can. Mineral.* **1981**, *19*, 3–17.
70. Irber, W. The Lanthanide Tetrad Effect and Its Correlation with K/Rb, Eu/Eu∗, Sr/Eu, Y/Ho, and Zr/Hf of Evolving Peraluminous Granite Suites. *Geochim. Cosmochim. Acta* **1999**, *63*, 489–508. [CrossRef]
71. Jochum, K.P.; Seufert, H.M.; Spettel, B.; Palme, H. The Solar-System Abundances of Nb, Ta, and Y, and the Relative Abundances of Refractory Lithophile Elements in Differentiated Planetary Bodies. *Geochim. Cosmochim. Acta* **1986**, *50*, 1173–1183. [CrossRef]
72. Weyer, S.; Münker, C.; Mezger, K. Nb/Ta, Zr/Hf and REE in the Depleted Mantle: Implications for the Differentiation History of the Crust–Mantle System. *Earth Planet. Sci. Lett.* **2003**, *205*, 309–324. [CrossRef]
73. Rudnick, R.L.; Fountain, D.M. Nature and Composition of the Continental Crust: A Lower Crustal Perspective. *Rev. Geophys.* **1995**, *33*, 267–309. [CrossRef]
74. Dostal, J.; Chatterjee, A.K. Contrasting Behaviour of Nb/Ta and Zr/Hf Ratios in a Peraluminous Granitic Pluton (Nova Scotia, Canada). *Chem. Geol.* **2000**, *163*, 207–218. [CrossRef]
75. David, K.; Schiano, P.; Allègre, C.J. Assessment of the Zr/Hf Fractionation in Oceanic Basalts and Continental Materials during Petrogenetic Processes. *Earth Planet. Sci. Lett.* **2000**, *178*, 285–301. [CrossRef]
76. Kamber, B.S.; Collerson, K.D. Role of 'Hidden' Deeply Subducted Slabs in Mantle Depletion. *Chem. Geol.* **2000**, *166*, 241–254. [CrossRef]
77. Eby, G.N. The A-Type Granitoids: A Review of Their Occurrence and Chemical Characteristics and Speculations on Their Petrogenesis. *Lithos* **1990**, *26*, 115–134. [CrossRef]
78. Münker, C.; Pfänder, J.A.; Weyer, S.; Büchl, A.; Kleine, T.; Mezger, K. Evolution of Planetary Cores and the Earth-Moon System from Nb/Ta Systematics. *Science* **2003**, *301*, 84–87. [CrossRef] [PubMed]
79. Pfänder, J.A.; Münker, C.; Stracke, A.; Mezger, K. Nb/Ta and Zr/Hf in Ocean Island Basalts—Implications for Crust–Mantle Differentiation and the Fate of Niobium. *Earth Planet. Sci. Lett.* **2007**, *254*, 158–172. [CrossRef]
80. Gale, A.; Dalton, C.A.; Langmuir, C.H.; Su, Y.; Schilling, J. The Mean Composition of Ocean Ridge Basalts. *Geochem Geophys Geosyst* **2013**, *14*, 489–518. [CrossRef]
81. Huang, H.; Niu, Y.; Zhao, Z.; Hei, H.; Zhu, D. On the Enigma of Nb-Ta and Zr-Hf Fractionation—A Critical Review. *J. Earth Sci.* **2011**, *22*, 52–66. [CrossRef]
82. Zhang, J.; Wang, R.; Hong, J.; Tang, M.; Zhu, D.-C. Nb-Ta Systematics of Kohistan and Gangdese Arc Lower Crust: Implications for Continental Crust Formation. *Ore Geol. Rev.* **2021**, *133*, 104131. [CrossRef]
83. Barth, M.G.; McDonough, W.F.; Rudnick, R.L. Tracking the Budget of Nb and Ta in the Continental Crust. *Chem. Geol.* **2000**, *165*, 197–213. [CrossRef]
84. Niu, Y. Earth Processes Cause Zr–Hf and Nb–Ta Fractionations, but Why and How? *RSC Adv.* **2012**, *2*, 3587–3591. [CrossRef]
85. Sun, S.-S.; McDonough, W.F. Chemical and Isotopic Systematics of Oceanic Basalts: Implications for Mantle Composition and Processes. *Geol. Soc. Lond. Spec. Publ.* **1989**, *42*, 313–345. [CrossRef]
86. Dorais, M.J.; Tubrett, M. Identification of a Subduction Zone Component in the Higganum Dike, Central Atlantic Magmatic Province: A LA-ICPMS Study of Clinopyroxene with Implications for Flood Basalt Petrogenesis. *Geochem. Geophys. Geosystems* **2008**, *9*, 1–13. [CrossRef]
87. Ma, L.; Wang, Q.; Li, Z.-X.; Wyman, D.A.; Yang, J.-H.; Jiang, Z.-Q.; Liu, Y.; Gou, G.-N.; Guo, H.-F. Subduction of Indian Continent beneath Southern Tibet in the Latest Eocene (~35Ma): Insights from the Quguosha Gabbros in Southern Lhasa Block. *Gondwana Res.* **2017**, *41*, 77–92. [CrossRef]
88. Zhu, C.Y.; Zhao, G.; Ji, J.; Sun, M.; Han, Y.; Liu, Q.; Eizenhöfer, P.R.; Zhang, X.; Hou, W. Subduction between the Jiamusi and Songliao Blocks: Geological, Geochronological and Geochemical Constraints from the Heilongjiang Complex. *Lithos* **2017**, *282–283*, 128–144. [CrossRef]
89. Jonnalagadda, M.K.; Karmalkar, N.R.; Duraiswami, R.A. Geochemistry of Eclogites of the Tso Morari Complex, Ladakh, NW Himalayas: Insights into Trace Element Behavior during Subduction and Exhumation. *Geosci. Front.* **2019**, *10*, 811–826. [CrossRef]
90. Chekol, T.; Meshesha, D.; Bululta, U. Petrogenesis and Geotectonic Setting of Berguda Granitoids of Neoproterozoic Burji-Finchawa Granite-Gneiss Complex, Southern Ethiopia: Implication for the Cessation of Subduction Control Magmatism in East African Orogeny. *Arab. J. Geosci.* **2022**, *15*, 732. [CrossRef]
91. Wilson, M. (Ed.) Geochemical Characteristics of Igneous Rocks as Petrogenetic Indicators. In *Igneous Petrogenesis*; Springer: Dordrecht, The Netherlands, 1989; pp. 13–35. ISBN 978-1-4020-6788-4.
92. McDonough, W.F.; Sun, S.-S. The Composition of the Earth. *Chem. Geol.* **1995**, *120*, 223–253. [CrossRef]
93. Witt-Eickschen, G.; Harte, B. Distribution of Trace Elements between Amphibole and Clinopyroxene from Mantle Peridotites of the Eifel (Western Germany): An Ion-Microprobe Study. *Chem. Geol.* **1994**, *117*, 235–250. [CrossRef]
94. Bachmann, O.; Dungan, M.A.; Bussy, F. Insights into Shallow Magmatic Processes in Large Silicic Magma Bodies: The Trace Element Record in the Fish Canyon Magma Body, Colorado. *Contrib. Miner. Petrol.* **2005**, *149*, 338–349. [CrossRef]
95. Farhan, M.; Arif, M.; Ying, Y.; Chen, X.; Garbe-Schönberg, D.; Li, C.-F.; Hussain, Z.; Ullah, Z.; Zhang, P.; Khan, A. Fluid Source, Element Mobility and Physicochemical Conditions of Porphyry-Style Hydrothermal Alteration-Mineralization at Mirkhani, Southern Chitral, Pakistan. *Ore Geol. Rev.* **2021**, *135*, 104222. [CrossRef]

96. Polat, A.; Longstaffe, F.; Weisener, C.; Fryer, B.; Frei, R.; Kerrich, R. Extreme Element Mobility during Transformation of Neoarchean (ca. 2.7Ga) Pillow Basalts to a Paleoproterozoic (ca. 1.9Ga) Paleosol, Schreiber Beach, Ontario, Canada. *Chem. Geol.* **2012**, *326–327*, 145–173. [CrossRef]
97. Pearce, J.A. Immobile Element Fingerprinting of Ophiolites. *Elements* **2014**, *10*, 101–108. [CrossRef]
98. Xiao, D.; Zhao, X.; Liao, Q.; Zhao, H.; Zeng, Z. Early Palaeozoic Arc-Related Gabbro-Diorite Suite in East Junggar, Southern Central Asian Orogenic Belt: Petrogenesis and Tectonic Implications. *Int. Geol. Rev.* **2020**, *62*, 1205–1223. [CrossRef]
99. Babechuk, M.G.; Widdowson, M.; Murphy, M.; Kamber, B.S. A Combined Y/Ho, High Field Strength Element (HFSE) and Nd Isotope Perspective on Basalt Weathering, Deccan Traps, India. *Chem. Geol.* **2015**, *396*, 25–41. [CrossRef]
100. Sampaio, G.M.S.; Pufahl, P.K.; Raye, U.; Kyser, K.T.; Abreu, A.T.; Alkmim, A.R.; Nalini, H.A. Influence of Weathering and Hydrothermal Alteration on the REE and δ56Fe Composition of Iron Formation, Cauê Formation, Iron Quadrangle, Brazil. *Chem. Geol.* **2018**, *497*, 27–40. [CrossRef]
101. Bobos, I.; Gomes, C. Mineralogy and Geochemistry (HFSE and REE) of the Present-Day Acid-Sulfate Types Alteration from the Active Hydrothermal System of Furnas Volcano, São Miguel Island, The Azores Archipelago. *Minerals* **2021**, *11*, 335. [CrossRef]
102. Darbandi, M.P.; Shafaroudi, A.M.; Karimpour, M.H.; Azimzadeh, A.M.; Klötzli, U.; Slama, J. The Gabbro-Diorite Magmatism from the Narm Area, Western Kuh-e-Sarhangi (Central Iran): Evolution from Eocene Magmatic Flare up to Miocene Asthenosphere Upwelling. *J. Afr. Earth Sci.* **2022**, *196*, 104692. [CrossRef]
103. Bau, M. Controls on the Fractionation of Isovalent Trace Elements in Magmatic and Aqueous Systems: Evidence from Y/Ho, Zr/Hf, and Lanthanide Tetrad Effect. *Contrib. Miner. Petrol.* **1996**, *123*, 323–333. [CrossRef]
104. Zhang, J.; Amakawa, H.; Nozaki, Y. The Comparative Behaviors of Yttrium and Lanthanides in the Seawater of the North Pacific. *Geophys. Res. Lett.* **1994**, *21*, 2677–2680. [CrossRef]
105. Ishikawa, Y.; Sawaguchi, T.; Iwaya, S.; Horiuchi, M. Delineation of Prospecting Targets for Kuroko Deposits Based on Modes of Volcanism of Underlying Dacite and Alteration Halos. *Min. Geol.* **1976**, *26*, 105–117.
106. Large, R.R.; Gemmell, J.B.; Paulick, H.; Huston, D.L. The Alteration Box Plot: A Simple Approach to Understanding the Relationship between Alteration Mineralogy and Lithogeochemistry Associated with Volcanic-Hosted Massive Sulfide Deposits. *Econ. Geol.* **2001**, *96*, 957–971. [CrossRef]
107. Watson, E.B.; Harrison, T.M. Zircon Saturation Revisited: Temperature and Composition Effects in a Variety of Crustal Magma Types. *Earth Planet. Sci. Lett.* **1983**, *64*, 295–304. [CrossRef]
108. Harrison, T.M.; Watson, E.B. The Behavior of Apatite during Crustal Anatexis: Equilibrium and Kinetic Considerations. *Geochim. Et Cosmochim. Acta* **1984**, *48*, 1467–1477. [CrossRef]
109. Ayers, J.C.; Watson, E.B.; Tarney, J.; Pickering, K.T.; Knipe, R.J.; Dewey, J.F. Solubility of Apatite, Monazite, Zircon, and Rutile in Supercritical Aqueous Fluids with Implications for Subduction Zone Geochemistry. *Philos. Trans. R. Soc. Lond. Ser. A Phys. Eng. Sci.* **1997**, *335*, 365–375. [CrossRef]
110. Bea, F.; Fershtater, G.; Corretgé, L.G. The Geochemistry of Phosphorus in Granite Rocks and the Effect of Aluminium. *Lithos* **1992**, *29*, 43–56. [CrossRef]
111. Pichavant, M.; Montel, J.-M.; Richard, L.R. Apatite Solubility in Peraluminous Liquids: Experimental Data and an Extension of the Harrison-Watson Model. *Geochim. Cosmochim. Acta* **1992**, *56*, 3855–3861. [CrossRef]
112. Montel, J.-M. A Model for Monazite/Melt Equilibrium and Application to the Generation of Granitic Magmas. *Chem. Geol.* **1993**, *110*, 127–146. [CrossRef]
113. Hayden, L.A.; Watson, E.B. Rutile Saturation in Hydrous Siliceous Melts and Its Bearing on Ti-Thermometry of Quartz and Zircon. *Earth Planet. Sci. Lett.* **2007**, *258*, 561–568. [CrossRef]
114. Gaetani, G.A.; Asimow, P.D.; Stolper, E.M. A Model for Rutile Saturation in Silicate Melts with Applications to Eclogite Partial Melting in Subduction Zones and Mantle Plumes. *Earth Planet. Sci. Lett.* **2008**, *272*, 720–729. [CrossRef]
115. Shao, T.; Xia, Y.; Ding, X.; Cai, Y.; Song, M. Zircon Saturation in Terrestrial Basaltic Melts and Its Geological Implications. *Solid Earth Sci.* **2019**, *4*, 27–42. [CrossRef]
116. Shao, T.; Xia, Y.; Ding, X.; Cai, Y.; Song, M. Zircon Saturation Model in Silicate Melts: A Review and Update. *Acta Geochim* **2020**, *39*, 387–403. [CrossRef]
117. Crisp, L.J.; Berry, A.J. A New Model for Zircon Saturation in Silicate Melts. *Contrib. Miner. Petrol.* **2022**, *177*, 71. [CrossRef]
118. Daneshvar, N.; Azizi, H.; Tsuboi, M. Estimating Magma Crystallization Temperatures Using High Field Strength Elements in Igneous Rocks. *Minerals* **2022**, *12*, 1260. [CrossRef]
119. Boehnke, P.; Watson, E.B.; Trail, D.; Harrison, T.M.; Schmitt, A.K. Zircon Saturation Re-Revisited. *Chem. Geol.* **2013**, *351*, 324–334. [CrossRef]
120. Gervasoni, F.; Klemme, S.; Rocha-Júnior, E.R.V.; Berndt, J. Zircon Saturation in Silicate Melts: A New and Improved Model for Aluminous and Alkaline Melts. *Contrib. Miner. Petrol.* **2016**, *171*, 21. [CrossRef]
121. Borisov, A.; Aranovich, L. Zircon Solubility in Silicate Melts: New Experiments and Probability of Zircon Crystallization in Deeply Evolved Basic Melts. *Chem. Geol.* **2019**, *510*, 103–112. [CrossRef]
122. Hoffman, S.; Mayne, M.J.; Stevens, G. Applying Phase Equilibria Modelling to Igneous Systems by Coupling Trace Element Partitioning and Accessory Phase Saturation to Compositionally Variable Thermodynamic Modelling in Rcrust. *Lithos* **2023**, *458–459*, 107335. [CrossRef]
123. Aranovich, L.Y.; Bortnikov, N.S. New Zr–Hf Geothermometer for Magmatic Zircons. *Petrology* **2018**, *26*, 115–120. [CrossRef]

124. Grimes, C.B.; Ushikubo, T.; John, B.E.; Valley, J.W. Uniformly Mantle-like δ18O in Zircons from Oceanic Plagiogranites and Gabbros. *Contrib. Miner. Petrol.* **2011**, *161*, 13–33. [CrossRef]
125. Yang, D.-G.; Sun, D.-Y.; Gou, J.; Hou, X.-G. Petrogenesis and Tectonic Setting of Carboniferous Hornblende Gabbros of the Northern Great Xing'an Range, NE China: Constraints from Geochronology, Geochemistry, Mineral Chemistry, and Zircon Hf Isotopes. *Geol. J.* **2018**, *53*, 2084–2098. [CrossRef]
126. Bea, F.; Bortnikov, N.; Cambeses, A.; Chakraborty, S.; Molina, J.F.; Montero, P.; Morales, I.; Silantiev, S.; Zinger, T. Zircon Crystallization in Low-Zr Mafic Magmas: Possible or Impossible? *Chem. Geol.* **2022**, *602*, 120898. [CrossRef]
127. Wolf, M.B.; London, D. Apatite Dissolution into Peraluminous Haplogranitic Melts: An Experimental Study of Solubilities and Mechanisms. *Geochim. Cosmochim. Acta* **1994**, *58*, 4127–4145. [CrossRef]
128. Piccoli, P.M.; Candela, P.A. Apatite in Igneous Systems. *Rev. Mineral. Geochem.* **2002**, *48*, 255–292. [CrossRef]
129. Webster, J.D.; Piccoli, P.M. Magmatic Apatite: A Powerful, Yet Deceptive, Mineral. *Elements* **2015**, *11*, 177–182. [CrossRef]
130. Yakymchuk, C. Behaviour of Apatite during Partial Melting of Metapelites and Consequences for Prograde Suprasolidus Monazite Growth. *Lithos* **2017**, *274–275*, 412–426. [CrossRef]
131. Williams, Q.; Hemley, R.J. Hydrogen in the Deep Earth. *Annu. Rev. Earth Planet. Sci.* **2001**, *29*, 365–418. [CrossRef]
132. Grove, T.L.; Till, C.B.; Krawczynski, M.J. The Role of H_2O in Subduction Zone Magmatism. *Annu. Rev. Earth Planet. Sci.* **2012**, *40*, 413–439. [CrossRef]
133. Murphy, J.B. Appinite Suites: A Record of the Role of Water in the Genesis, Transport, Emplacement and Crystallization of Magma. *Earth-Sci. Rev.* **2013**, *119*, 35–59. [CrossRef]
134. Ma, X.; Xu, Z.; Zhao, Z.; Yi, Z. Identification of a New Source for the Triassic Langjiexue Group: Evidence from a Gabbro-Diorite Complex in the Gangdese Magmatic Belt and Zircon Microstructures from Sandstones in the Tethyan Himalaya, Southern Tibet. *Geosphere* **2020**, *16*, 407–434. [CrossRef]
135. Nakamura, H.; Iwamori, H.; Nakagawa, M.; Shibata, T.; Kimura, J.-I.; Miyazaki, T.; Chang, Q.; Vaglarov, B.S.; Takahashi, T.; Hirahara, Y. Geochemical Mapping of Slab-Derived Fluid and Source Mantle along Japan Arcs. *Gondwana Res.* **2019**, *70*, 36–49. [CrossRef]
136. De Hoog, J.; Clarke, E.; Hattori, K. Mantle Wedge Olivine Modifies Slab-Derived Fluids: Implications for Fluid Transport from Slab to Arc Magma Source. *Geology* **2023**, *51*, 663–667. [CrossRef]
137. Pearce, J.A. Role of the Sub-Continental Lithosphere in Magma Genesis at Active Continental Margins. In *Continental Basalts and Mantle Xenoliths*; Hawkesworth, C.J., Norry, M.J., Eds.; Shiva Publications: Cheshire, UK, 1983; pp. 230–249. ISBN 978-0-906812-34-1.
138. Pearce, J.A.; Peate, D.W. Tectonic Implications of the Composition of Volcanic ARC Magmas. *Annu. Rev. Earth Planet. Sci.* **1995**, *23*, 251–285. [CrossRef]
139. Turner, S.J.; Langmuir, C.H. The Global Chemical Systematics of Arc Front Stratovolcanoes: Evaluating the Role of Crustal Processes. *Earth Planet. Sci. Lett.* **2015**, *422*, 182–193. [CrossRef]
140. Wood, D.A. The Application of a ThHfTa Diagram to Problems of Tectonomagmatic Classification and to Establishing the Nature of Crustal Contamination of Basaltic Lavas of the British Tertiary Volcanic Province. *Earth Planet. Sci. Lett.* **1980**, *50*, 11–30. [CrossRef]
141. Hollocher, K.; Robinson, P.; Walsh, E.; Roberts, D. Geochemistry of Amphibolite-Facies Volcanics and Gabbros of the Støren Nappe in Extensions West and Southwest of Trondheim, Western Gneiss Region, Norway: A Key to Correlations and Paleotectonic Settings. *Am. J. Sci.* **2012**, *312*, 357–416. [CrossRef]
142. Pearce, J.A.; Harris, N.B.W.; Tindle, A.G. Trace Element Discrimination Diagrams for the Tectonic Interpretation of Granitic Rocks. *J. Petrol.* **1984**, *25*, 956–983. [CrossRef]
143. Defant, M.J.; Drummond, M.S. Mount St. Helens: Potential Example of the Partial Melting of the Subducted Lithosphere in a Volcanic Arc. *Geology* **1993**, *21*, 547–550. [CrossRef]
144. Marschall, H.R.; Schumacher, J.C. Arc Magmas Sourced from Mélange Diapirs in Subduction Zones. *Nat. Geosci.* **2012**, *5*, 862–867. [CrossRef]
145. Zheng, Y.-F.; Chen, Y.-X. Continental versus Oceanic Subduction Zones. *Natl. Sci. Rev.* **2016**, *3*, 495–519. [CrossRef]
146. Zheng, Y.-F. Subduction Zone Geochemistry. *Geosci. Front.* **2019**, *10*, 1223–1254. [CrossRef]
147. Li, H.; Hermann, J.; Zhang, L. Melting of Subducted Slab Dictates Trace Element Recycling in Global Arcs. *Sci. Adv.* **2022**, *8*, eabh2166. [CrossRef]
148. Castillo, P.R. An Alternative New View of Convergent Margin Magmatism. *J. Asian Earth Sci.* **2023**, *256*, 105834. [CrossRef]
149. Hawkesworth, C.J.; Hergt, J.M.; Ellam, R.M.; Dermott, F.M. Element Fluxes Associated with Subduction Related Magmatism. *Philos. Trans. Phys. Sci. Eng.* **1991**, *335*, 393–405.
150. Schmidt, M.W.; Jagoutz, O. The Global Systematics of Primitive Arc Melts. *Geochem. Geophys. Geosystems* **2017**, *18*, 2817–2854. [CrossRef]
151. Turner, S.J.; Langmuir, C.H.; Dungan, M.A.; Escrig, S. The Importance of Mantle Wedge Heterogeneity to Subduction Zone Magmatism and the Origin of EM1. *Earth Planet. Sci. Lett.* **2017**, *472*, 216–228. [CrossRef]
152. Lee, C.-T.A.; Cheng, X.; Horodyskyj, U. The Development and Refinement of Continental Arcs by Primary Basaltic Magmatism, Garnet Pyroxenite Accumulation, Basaltic Recharge and Delamination: Insights from the Sierra Nevada, California. *Contrib. Miner. Petrol.* **2006**, *151*, 222–242. [CrossRef]

153. Wood, B.; Kiseeva, K.; Matzen, A. Garnet in the Earth's Mantle. *Elements* **2013**, *9*, 421–426. [CrossRef]
154. Taylor, S.R.; McClennan, S.M. *The Continental Crust: Its Composition and Evolution: An Examination of the Geochemical Record Preserved in Sedimentary Rocks*; Geoscience Texts; Blackwell Scientific: Oxford, UK, 1985; ISBN 978-0-632-01148-3.
155. Hofmann, A.W. Chemical Differentiation of the Earth: The Relationship between Mantle, Continental Crust, and Oceanic Crust. *Earth Planet. Sci. Lett.* **1988**, *90*, 297–314. [CrossRef]
156. Salters, V.J.M.; Stracke, A. Composition of the Depleted Mantle. *Geochem. Geophys. Geosystems* **2004**, *5*, 1–27. [CrossRef]
157. Wedepohl, K. The Composition of the Continental Crust. *Geochim. Et Cosmochim. Acta* **1995**, *59*, 1217–1232. [CrossRef]
158. Hofmann, A.W.; White, W.M. Ba, Rb and Cs in the Earth's Mantle. *Z. Für Naturforschung A* **1983**, *38*, 256–266. [CrossRef]
159. Green, T.H. Significance of Nb/Ta as an Indicator of Geochemical Processes in the Crust-Mantle System. *Chem. Geol.* **1995**, *120*, 347–359. [CrossRef]
160. Smith, E.I.; Sánchez, A.; Walker, J.D.; Wang, K. Geochemistry of Mafic Magmas in the Hurricane Volcanic Field, Utah: Implications for Small- and Large-Scale Chemical Variability of the Lithospheric Mantle. *J. Geol.* **1999**, *107*, 433–448. [CrossRef]
161. Robinson, J.A.C.; Wood, B.J. The Depth of the Spinel to Garnet Transition at the Peridotite Solidus. *Earth Planet. Sci. Lett.* **1998**, *164*, 277–284. [CrossRef]
162. Su, B.; Zhang, H.; Asamoah, S.P.; Qin, K.; Tang, Y.; Ying, J.; Xiao, Y. Garnet-Spinel Transition in the Upper Mantle: Review and Interpretation. *J. Earth Sci.* **2010**, *21*, 635–640. [CrossRef]
163. Fram, M.S.; Lesher, C.E. Geochemical Constraints on Mantle Melting during Creation of the North Atlantic Basin. *Nature* **1993**, *363*, 712–715. [CrossRef]
164. Mayborn, K.R.; Lesher, C.E. Paleoproterozoic Mafic Dike Swarms of Northeast Laurentia: Products of Plumes or Ambient Mantle? *Earth Planet. Sci. Lett.* **2004**, *225*, 305–317. [CrossRef]
165. Duggen, S.; Hoernle, K.; van den Bogaard, P.; Garbe-Schönberg, D. Post-Collisional Transition from Subduction- to Intraplate-Type Magmatism in the Westernmost Mediterranean: Evidence for Continental-Edge Delamination of Subcontinental Lithosphere. *J. Petrol.* **2005**, *46*, 1155–1201. [CrossRef]
166. Jiang, Y.-H.; Jia, R.-Y.; Liu, Z.; Liao, S.-Y.; Zhao, P.; Zhou, Q. Origin of Middle Triassic High-K Calc-Alkaline Granitoids and Their Potassic Microgranular Enclaves from the Western Kunlun Orogen, Northwest China: A Record of the Closure of Paleo-Tethys. *Lithos* **2013**, *156–159*, 13–30. [CrossRef]
167. Liu, Y.; Zhang, Y.; Sun, J.; Xu, Z.; Liu, Y.; Zhang, X.; Pan, Y.; Han, J.; Chu, X. Petrology, Geochemistry, and Zircon U–Pb Isotopes of Xintian Complex in Yanbian Area, Northeast China: Evidence for Magma Mixing and Geodynamics Processes. *Geol. J.* **2020**, *55*, 5417–5431. [CrossRef]
168. Hawkesworth, C.J.; Gallagher, K.; Hergt, J.M.; McDermott, F. Mantle and Slab Contributions in ARC Magmas. *Annu. Rev. Earth Planet. Sci.* **1993**, *21*, 175–204. [CrossRef]
169. Mallik, A.; Nelson, J.; Dasgupta, R. Partial Melting of Fertile Peridotite Fluxed by Hydrous Rhyolitic Melt at 2–3 GPa: Implications for Mantle Wedge Hybridization by Sediment Melt and Generation of Ultrapotassic Magmas in Convergent Margins. *Contrib. Miner. Petrol.* **2015**, *169*, 48. [CrossRef]
170. Grove, T.L.; Till, C.B. H_2O-Rich Mantle Melting near the Slab–Wedge Interface. *Contrib. Miner. Petrol.* **2019**, *174*, 80. [CrossRef]
171. Class, C.; Miller, D.M.; Goldstein, S.L.; Langmuir, C.H. Distinguishing Melt and Fluid Subduction Components in Umnak Volcanics, Aleutian Arc. *Geochem. Geophys. Geosystems* **2000**, *1*, 1–28. [CrossRef]
172. Hanyu, T.; Tatsumi, Y.; Nakai, S.; Chang, Q.; Miyazaki, T.; Sato, K.; Tani, K.; Shibata, T.; Yoshida, T. Contribution of Slab Melting and Slab Dehydration to Magmatism in the NE Japan Arc for the Last 25 Myr: Constraints from Geochemistry. *Geochem. Geophys. Geosystems* **2006**, *7*, 1–29. [CrossRef]
173. Walowski, K.J.; Wallace, P.J.; Clynne, M.A.; Rasmussen, D.J.; Weis, D. Slab Melting and Magma Formation beneath the Southern Cascade Arc. *Earth Planet. Sci. Lett.* **2016**, *446*, 100–112. [CrossRef]
174. Zhao, L.; Guo, F.; Fan, W.; Huang, M. Roles of Subducted Pelagic and Terrigenous Sediments in Early Jurassic Mafic Magmatism in NE China: Constraints on the Architecture of Paleo-Pacific Subduction Zone. *J. Geophys. Res. Solid Earth* **2019**, *124*, 2525–2550. [CrossRef]
175. Pearce, J.A. Geochemical Fingerprinting of Oceanic Basalts with Applications to Ophiolite Classification and the Search for Archean Oceanic Crust. *Lithos* **2008**, *100*, 14–48. [CrossRef]
176. Ellam, R.M.; Hawkesworth, C.J. Elemental and Isotopic Variations in Subduction Related Basalts: Evidence for a Three Component Model. *Contrib. Mineral. Petrol.* **1988**, *98*, 72–80. [CrossRef]
177. Brenan, J.M.; Shaw, H.F.; Ryerson, F.J.; Phinney, D.L. Mineral-Aqueous Fluid Partitioning of Trace Elements at 900 °C and 2.0 GPa: Constraints on the Trace Element Chemistry of Mantle and Deep Crustal Fluids. *Geochim. Et Cosmochim. Acta* **1995**, *59*, 3331–3350. [CrossRef]
178. Lee, C.A. Trace Element Evidence for Hydrous Metasomatism at the Base of the North American Lithosphere and Possible Association with Laramide Low-Angle Subduction. *J. Geol.* **2005**, *113*, 673–685. [CrossRef]
179. Woodhead, J.D.; Hergt, J.M.; Davidson, J.P.; Eggins, S.M. Hafnium Isotope Evidence for 'Conservative' Element Mobility during Subduction Zone Processes. *Earth Planet. Sci. Lett.* **2001**, *192*, 331–346. [CrossRef]
180. Zhao, Z.; Mo, X.; Dilek, Y.; Niu, Y.; DePaolo, D.J.; Robinson, P.; Zhu, D.; Sun, C.; Dong, G.; Zhou, S.; et al. Geochemical and Sr–Nd–Pb–O Isotopic Compositions of the Post-Collisional Ultrapotassic Magmatism in SW Tibet: Petrogenesis and Implications for India Intra-Continental Subduction beneath Southern Tibet. *Lithos* **2009**, *113*, 190–212. [CrossRef]

181. Hoffer, G.; Eissen, J.-P.; Beate, B.; Bourdon, E.; Fornari, M.; Cotten, J. Geochemical and Petrological Constraints on Rear-Arc Magma Genesis Processes in Ecuador: The Puyo Cones and Mera Lavas Volcanic Formations. *J. Volcanol. Geotherm. Res.* **2008**, *176*, 107–118. [CrossRef]
182. Miao, Z.; Li, X.; Zhao, Z.; Niu, Y.; Xu, B.; Lei, H.; Wu, J.; Yang, Y.; Ma, Q.; Liu, D.; et al. Deciphering Mantle Heterogeneity Associated with Ancient Subduction-Related Metasomatism: Insights from Mg-K Isotopes in Potassic Alkaline Rocks. *Geochim. Et Cosmochim. Acta* **2023**, *348*, 258–277. [CrossRef]
183. Thompson, R.N.; Morrison, M.A.; Mattey, D.P.; Dickin, A.P.; Moorbath, S. An Assessment of the ThHfTa Diagram as a Discriminant for Tectonomagmatic Classifications and in the Detection of Crustal Contamination of Magmas. *Earth Planet. Sci. Lett.* **1980**, *50*, 1–10. [CrossRef]
184. Shellnutt, J.; Wang, C.Y.; Zhou, M.-F.; Yang, Y. Zircon Lu–Hf Isotopic Compositions of Metaluminous and Peralkaline A-Type Granitic Plutons of the Emeishan Large Igneous Province (SW China): Constraints on the Mantle Source. *J. Asian Earth Sci.* **2009**, *35*, 45–55. [CrossRef]
185. Davidson, J.P.; Wilson, I.R. Evolution of an Alkali Basalt—Trachyte Suite from Jebel Marra Volcano, Sudan, through Assimilation and Fractional Crystallization. *Earth Planet. Sci. Lett.* **1989**, *95*, 141–160. [CrossRef]
186. Hofmann, A.W.; Jochum, K.P.; Seufert, M.; White, W.M. Nb and Pb in Oceanic Basalts: New Constraints on Mantle Evolution. *Earth Planet. Sci. Lett.* **1986**, *79*, 33–45. [CrossRef]
187. Choi, H.-O.; Choi, S.H.; Lee, Y.S.; Ryu, J.-S.; Lee, D.-C.; Lee, S.-G.; Sohn, Y.K.; Liu, J. Petrogenesis and Mantle Source Characteristics of the Late Cenozoic Baekdusan (Changbaishan) Basalts, North China Craton. *Gondwana Res.* **2020**, *78*, 156–171. [CrossRef]
188. González-Luz, S.; Arce, J.L.; Macías, J.L.; Schaaf, P. Origin and Crustal Contamination of Magmas of the Chiapanecan Volcanic Arc in Southern Mexico: Constraints from New Geochemical, Isotopic, and Geochronologic Data. *Lithos* **2023**, *442–443*, 107060. [CrossRef]
189. Slezak, P.; Hitzman, M.W.; van Acken, D.; Dunlevy, E.; Chew, D.; Drakou, F.; Holdstock, M. Petrogenesis of the Limerick Igneous Suite: Insights into the Causes of Post-Eruptive Alteration and the Magmatic Sources Underlying the Iapetus Suture in SW Ireland. *J. Geol. Soc.* **2023**, *180*, jgs2022-039. [CrossRef]

Disclaimer/Publisher's Note: The statements, opinions and data contained in all publications are solely those of the individual author(s) and contributor(s) and not of MDPI and/or the editor(s). MDPI and/or the editor(s) disclaim responsibility for any injury to people or property resulting from any ideas, methods, instructions or products referred to in the content.